JOURNAL OF GEOPHYSICAL RESEARCH, VOL. 99, NO. B12, PAGES 24,135–24,157, DECEMBER 10, 1994

Tomographic imaging of the shallow crustal structure of the East Pacific Rise at 9°30'N

Douglas R. Toomey
Department of Geological Sciences, University of Oregon, Eugene

Sean C. Solomon
Department of Terrestrial Magnetism, Carnegie Institution of Washington, Washington, D. C.

G. M. Purdy
Department of Geology and Geophysics, Woods Hole Oceanographic Institution, Woods Hole, Massachusetts

Abstract. Compressional wave travel times from a seismic tomography experiment at 9°30'N on the East Pacific Rise are analyzed by a new tomographic method to determine the three-dimensional seismic velocity structure of the upper 2.5 km of oceanic crust within a 20 x 18 km^2 area centered on the rise axis. The data comprise the travel times and associated uncertainties of 1459 compressional waves that have propagated above the axial magma chamber. A careful analysis of source and receiver parameters, in conjunction with an automated method of picking *P* wave onsets and assigning uncertainties, constrains the prior uncertainty in the data to 5 to 20 ms. The new tomographic method employs graph theory to estimate ray paths and travel times through strongly heterogeneous and densely parameterized seismic velocity models. The nonlinear inverse method uses a jumping strategy to minimize a functional that includes the penalty function, horizontal and vertical smoothing constraints, and prior model assumptions; all constraints applied to model perturbations are normalized to remove bias. We use the tomographic method to reject the null hypothesis that the axial seismic structure is two-dimensional. Three-dimensional models reveal a seismic structure that correlates well with cross- and along-axis variations in seafloor morphology, the location of the axial summit caldera, and the distribution of seafloor hydrothermal activity. The along-axis segmentation of the seismic structure above the axial magma chamber is consistent with the hypothesis that mantle-derived melt is preferentially injected midway along a locally linear segment of the rise and that the architecture of the crustal section is characterized by an en echelon series of elongate axial volcanoes approximately 10 km in length. The seismic data are compatible with a 300- to 500-m-thick thermal anomaly above a midcrustal melt lens; such an interpretation suggests that hydrothermal fluids may not have penetrated this region in the last 10^3 years. Asymmetries in the seismic structure across the rise support the inferences that the thickness of seismic layer 2 and the average midcrustal temperature increase to the west of the rise axis. These anomalies may be the result of off-axis magmatism; alternatively, the asymmetric thermal anomaly may be the consequence of differences in the depth extent of hydrothermal cooling.

Introduction

Marine seismology has made considerable recent progress toward an improved definition and understanding of the structure of oceanic crust in the vicinity of mid-ocean ridges. Much of this progress has come from focusing a range of seismic experiments on individual sections of the ridge system and thereby accumulating independent and complementary constraints on physical structure. The East Pacific Rise (EPR) near 9°30'N is a noteworthy example of a section of a fast spreading center that has served as such a focus. Multichannel seismic (MCS) reflection profiling has yielded constraints on the cross-axis width and depth of a strong midcrustal reflector interpreted as the top of the axial magma chamber (AMC) [*Detrick et al.*, 1987; *Kent et al.*, 1990, 1993] and has imaged the cross-axis structure of the shallowest volcanic layers [*Harding et al.*, 1993]. Rise-parallel refraction experiments, using the expanding-spread profile method, have provided one-dimensional velocity-depth distributions at several discrete crustal ages [*Vera et al.*, 1990]. On-bottom seismic refraction experiments, conducted along and across the rise summit, have yielded detailed two-dimensional models of the uppermost crust [*Christeson et al.*, 1992]. Last, a three-dimensional tomographic experiment has imaged pronounced anomalies in compressional wave velocity and attenuation at all crustal depths, including the low-velocity, low-*Q* volume that envelops the AMC reflector observed on MCS profiles [*Toomey et al.*, 1990; *Wilcock et al.*, 1992b, submitted manuscript]. The results of all of the seismic experiments at 9°30'N and more limited studies along other sections of the EPR [e.g., *McClain et al.*, 1985; *Harding et al.*, 1989; *Caress et al.*, 1992; *Detrick et al.*, 1993; *Kent et al.*, 1994] have led to the development of new working models for axial magma chambers and crustal formational processes along fast spread-

Paper number 94JB01942.
0148-0227/94/94JB-01942$05.00

ing mid-ocean ridges [e.g., *Sinton and Detrick*, 1992; *Solomon and Toomey*, 1992].

Seismic imaging of mid-ocean ridge structure provides an opportunity to address the coupled processes of magma chamber evolution and hydrothermal circulation. Between the mid-crustal magma reservoir and the venting at the seafloor of high-temperature sulfide-rich fluids lies a 1- to 2-km-thick zone where physical properties such as temperature and permeability play a critical role in the development and evolution of hydrothermal flow patterns. Seismic parameters, which include the velocity and attenuation of compressional and shear wave energy, are particularly sensitive to variations in temperature and porosity at scales of seismic wavelengths and greater. Thus we can expect that fresh constraints on the three-dimensional seismic structure of newly formed oceanic crust will provide new insights into the relationships between magmatic and hydrothermal regimes.

In this paper we develop a new tomographic method whose accuracy and robustness surpass those of methods previously applied to mid-ocean ridge seismic data sets. The improved accuracy of the method permits new information to be obtained from the seismic tomography data from 9°30'N [*Toomey et al.*, 1990]. From a high-quality subset of the compressional wave travel time data we focus the tomographic analysis on the two- and three-dimensional structure of the crust immediately above the axial magma chamber and the off-axis structure above 2.5 km depth. Within this shallow crustal region we find that the seismic structure is fully three-dimensional and that the variations in compressional wave velocity correlate well with variations in the seafloor morphology, the location and form of the axial summit caldera (ASC), and the distribution of high-temperature seafloor hydrothermal venting.

Experiment Description

The objective of the 1988 seismic tomography experiment at 9°30'N was to image the three-dimensional crustal seismic structure of a fast spreading mid-ocean ridge. Figure 1 shows that this section of the EPR is uninterrupted by overlapping spreading centers or large off-axis seamounts and that the rise summit is easily identified as a continuous bathymetric high which gradually deepens toward the south. This section of the EPR has been the site of a variety of seafloor mapping [e.g., *Haymon et al.*, 1991; *Fornari et al.*, 1992; *Wilcock et al.*, 1993a] and geochemical sampling surveys [e.g., *Langmuir et al.*, 1986; *Perfit et al.*, 1994], as well as diverse seismic experiments [e.g., *Detrick et al.*, 1987; *Vera et al.*, 1990; *Vera and Diebold*, 1994; *Kent et al.*, 1990, 1993; *Toomey et al.*, 1990; *Christeson et al.*, 1992; *Wilcock et al.*, 1992b, 1993b; *Harding et al.*, 1993] .

We deployed an array of 15 ocean bottom receivers within a 30 x 40 km^2 area centered on the rise axis to record seismic energy from nearly 500 explosive sources (Figure 1). Eight of the instruments were continuously recording analog ocean bottom hydrophones (AOBHs) [*Koelsch and Purdy*, 1979], five were digital ocean bottom hydrophones (DOBHs) [*Koelsch et al.*, 1982] that operated in triggered mode, and two were three-component ocean bottom seismometers (OBSs) [*Mattaboni and Solomon*, 1977] that recorded digital data, also in a triggered mode. All 15 instruments recorded usable data; however, one AOBH located 20 km to the east of the rise axis recorded only water wave phases.

Each seismic source was a 120-lb. explosive charge tethered to a surface float to ensure a fixed depth of detonation at 69 m below sea level. Because of the uniform size, packaging, and depth of detonation, the source signature for these charges was effectively identical, ensuring that any variability in the recorded data is the result of either known instrument response or the effects of seismic propagation [*Wilcock et al.*, submitted manuscript]. A total of 482 explosive charges were detonated, of which 462 were well-recorded by most instruments. The primary shooting area encompassed a 16 x 16 km^2 area centered on the rise axis. Within this region the shot spacing was nominally 1 km, except that within 3 km of the rise axis the shot spacing was decreased to approximately 0.5 km. The experiment was designed to permit tomographic mapping of structure within the primary shooting area and between the seafloor and the crust-mantle transition. The OBHs and the DOBHs recorded almost all, and the OBSs about 80%, of the explosive seismic sources. In addition, the continuously recording AOBHs provided records of nearby microearthquakes [*Wilcock et al.*, 1992a] and several air gun profiles [*Christeson*, 1994].

Delay time seismic tomography relies on small differences among observed travel times to detect changes in structure. Thus an important step in our analysis of the data was the estimation of source and receiver positions and source origin times; the procedures we followed for source and receiver relocation are outlined in the appendix. Table 1 lists the final instrument locations and their uncertainties. For the seismic tomography analysis that follows, we used data only from sources whose parameters were constrained by five or more observations. For this subset of sources, the formal estimates of the uncertainty in shot position and origin time were typically less than 10 m and 5 ms, respectively.

Arrival Time Data

The tomographic imaging of seismic velocity structure requires observations of phase arrival times as well as reliable estimates of the uncertainty in these times. Typically, these quantities are prescribed subjectively by visual methods. A shortcoming of such an approach, however, is that for data sets that number in the thousands it is difficult to achieve an internally consistent assignment of data uncertainty from the first to the last visual pick. Because of this difficulty, and because of the importance of relative uncertainty estimates to imaging methods that use a least squares minimization criterion, we have developed automated methods for the estimation of both phase onset time and uncertainty.

We used the autoregressive method of *Takanami and Kitagawa* [1988] to identify the onset time of compressional wave arrivals. In this technique, a systematic search for the onset time is accomplished by optimizing the fit of two autoregressive models to the seismic data. On the assumption that the noise preceding a seismic event and the event itself represent two locally stationary time series, the method defines the arrival time as the boundary that best separates the two stochastic processes. The location of this boundary is found by a minimization criterion [*Takanami and Kitagawa*, 1988]. An example of the procedure applied to a seismogram recorded during the tomography experiment, including a graph of the AIC (Akaike Information Criterion [*Takanami and Kitagawa*, 1988]), is shown in Figure 2. The *P* wave arrival time is identified by the global minimum of the AIC. We also

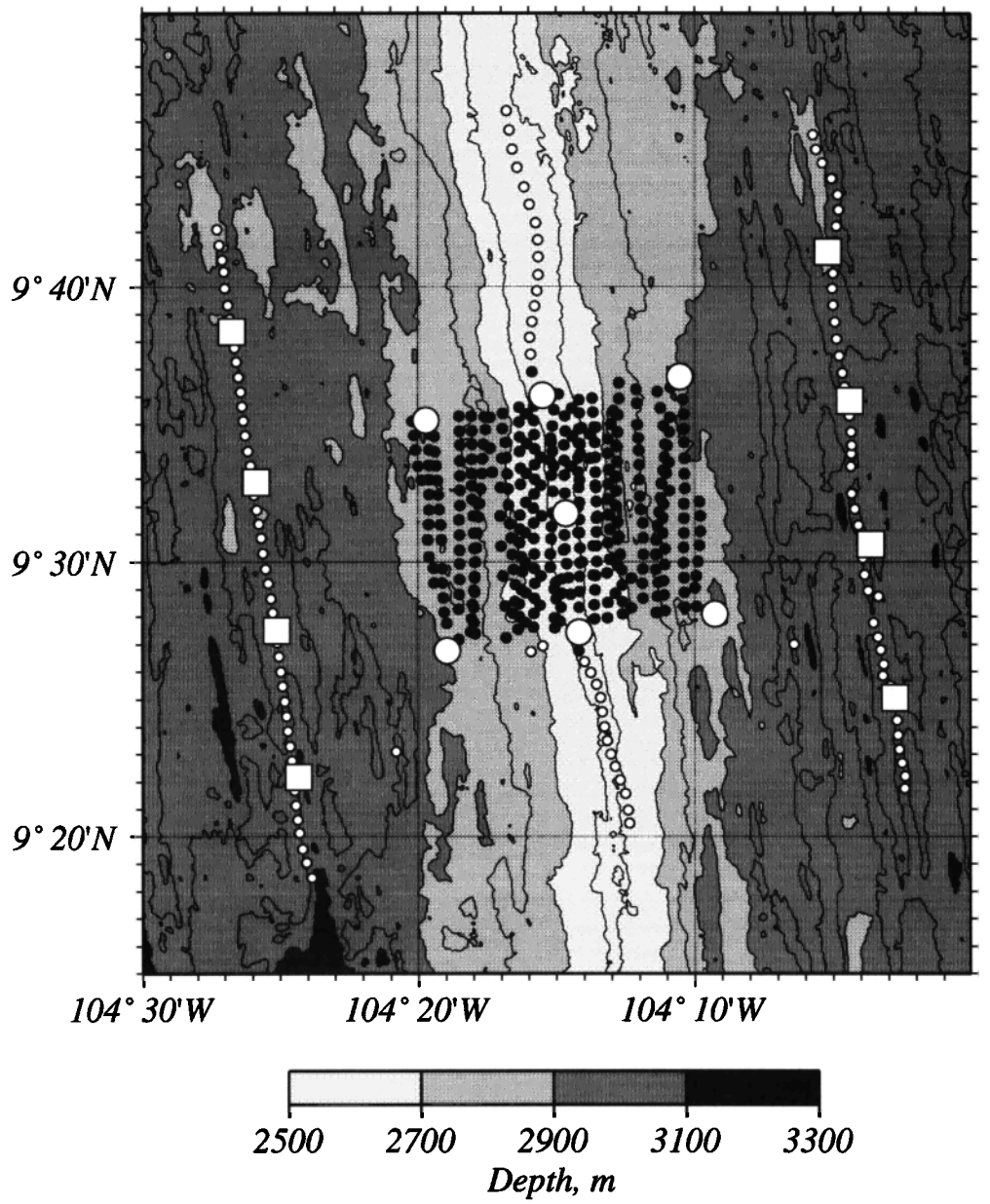

Figure 1. Bathymetry of the East Pacific Rise in the vicinity of the tomography experiment [from *Wilcock et al.*, 1993a]; 50-m contour interval. The positions of the 15 ocean bottom receivers (larger symbols) and the 480 explosive sources (smaller symbols) are shown. The subsets of sources and receivers used in this study are indicated by small solid circles and large open circles, respectively.

sought a means for estimating the arrival time uncertainty by characterizing the shape of the misfit function. To do this exactly is a difficult problem since autoregressive methods are nonlinear. Consequently, we made the simplifying assumption that the variation in the uncertainty in an arrival time is inversely proportional to the local gradient of the AIC function. By trial and error we determined the range of AIC values, relative to the minimum of the AIC function, that corresponded to the range of plausible arrival times. This was done for several instruments and several hundred seismograms, and it was found that an increase in the visually defined estimates of uncertainty correlated well with a decrease in the local gradient of the AIC function. Relative to the minimum AIC value, we chose a threshold value that separated the range of probable arrival times from improbable ones. Our estimate of uncertainty was taken as simply half the length of the time window associated with the AIC values that were less than the threshold. Admittedly, this approach is inexact and to some degree arbitrary in terms of assigning an absolute level of uncertainty. However, it does have the advantage that the relative variation in the estimates of arrival time uncertainty are assigned in an objective fashion, thus removing the variability intrinsic to subjective visual methods.

The relative uncertainties derived from the autoregressive method can be scaled to achieve absolute levels of uncertainty using the results of source and receiver relocation. The value of the rms residual for the water wave arrival time data following instrument and shot relocation (5 ms) gives an objective

Table 1. Instrument Positions

Instrument	Latitude, N	Longitude, W	Depth, m	σ_x, m	σ_y, m	σ_z, m
AOBH1	9°32.899'	104°25.861'	2922	11	10	10
AOBH2	9°27.509'	104°25.116'	2961	10	9	10
AOBH3	9°31.740'	104°14.656'	2579	8	9	10
AOBH4	9°26.765'	104°18.940'	2888	8	8	10
AOBH5	9°27.433'	104°14.169'	2595	8	10	10
AOBH6	9°28.087'	104°09.259'	2893	9	13	10
AOBH7	9°35.842'	104°04.391'	3056	12	18	10
AOBH8	9°30.613'	104°03.637'	3013	10	19	10
DOBH10	9°38.357'	104°26.735'	2949	18	13	10
DOBH12	9°22.164'	104°24.336'	3120	15	10	10
DOBH13	9°41.276'	104°05.183'	2918	22	20	10
DOBH14	9°25.058'	104°02.770'	3029	16	23	10
DOBH15	9°36.721'	104°10.529'	2901	12	12	10
DOBS31	9°36.028'	104°15.495'	2563	11	11	10
DOBS33	9°35.126'	104°19.705'	2895	10	9	10

σ_x, σ_y, and σ_z are the uncertainties in longitude, latitude, and depth, respectively.

estimate of the expected uncertainty in the onset time of impulsive *P* waves. This inference follows because the speed of sound in water is well known and because the data used to relocate the instruments are affected by the same uncertainties as the data used in the tomographic analysis. These error sources include (1) imperfectly known source and receiver parameters and clock corrections and (2) misidentification of the phase onset time. The relative uncertainties in the arrival times of impulsive *P* waves, as calculated by the automated picking methods, were thus rescaled so that the minimum possible value was also 5 ms. For the data satisfying the selection criteria outlined below, the range of uncertainty in the P wave arrival times after rescaling was 5-20 ms.

Because the present study focuses on shallow crustal structure, the full set of first-arriving *P* wave data was winnowed to ensure that all phases were associated with propagation paths that did not significantly interact with the axial magmatic system (Figure 3). This criterion ensures that the geometry of the seismic ray paths are well behaved and that the character of the first-arriving phase is generally impulsive; diffracted arrivals are not included in this study. Our reason for limiting the subset of data is that the anticipated variations in shallow crustal seismic structure are predicted to give rise to travel time residuals that are small in comparison with those resulting from propagation around or through the axial magmatic system. Because least squares inversions preferentially attempt to minimize the largest misfit, which is expected to be associated with the axial magma chamber, a simultaneous analysis of the complete data set would limit our ability to resolve the fine-scale variation in the shallowest crustal structure. The data were further winnowed by eliminating paths with source or receiver positions that lie beyond 10 km of the rise axis (Figure 1), thus avoiding complications that might arise due to variations in structure that occur beyond the region of primary shooting.

The quality of the *P* wave travel time data employed in the present tomographic analysis is remarkably high. In addition to the causes of uncertainty in the arrival time of a *P* wave outlined above, the only other source of potential misfit, excluding that due to unknown structure, is noise due to imprecisely known seafloor bathymetry. For a slowness contrast across the seafloor boundary of 0.33 s/km and an uncertainty in the water depths of 10 m [*Wilcock et al.*, 1993a], the resulting uncertainty in travel time due to seafloor bathymetry is approximately 3 ms. Thus if the crustal structure were perfectly known, we could expect the final rms *P* wave travel time residual to be 6 ms.

Tomographic Method

The tomographic imaging of mid-ocean ridges is particularly demanding because of the large magnitude and the frequently short length scales of the seismic heterogeneity. An illustrative two-dimensional model of the seismic structure beneath the East Pacific Rise, derived from a one-dimensional analysis of rise-parallel refraction lines and cross-axis reflection data [*Vera et al.*, 1990], is shown in Figure 3. The principal sources of heterogeneity in the seismic model are the rough seafloor, with a velocity contrast of 1-3 km/s, and the axial magmatic system, where lateral velocity variations exceed 50% over distances of a few kilometers. The complexity of the seismic structure that typifies mid-ocean ridges has several implications for both the forward and inverse components of a tomographic algorithm [*Hole*, 1992]. To reproduce simply the velocity structure of Figure 3b requires a densely parameterized model. The use of a nodal parameterization and a spacing between nodes of 200 m in both the vertical and horizontal directions, for example, requires over 2500 model pa-

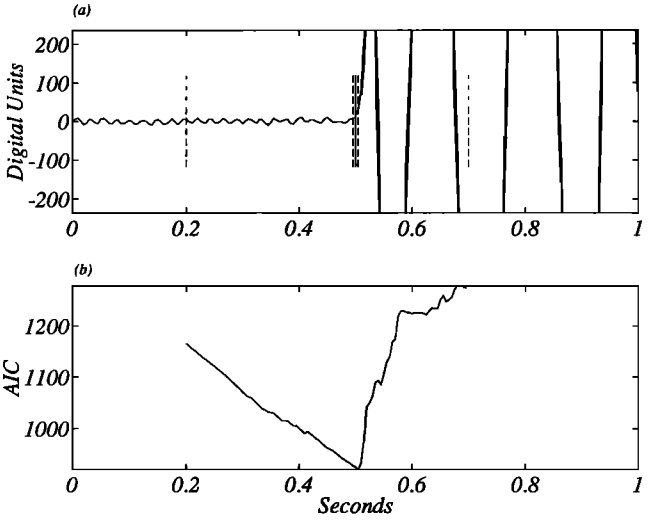

Figure 2. An example of the automated identification of the *P* wave onset and arrival time uncertainty. (a) Seismogram recorded by an ocean bottom receiver at a range of 10 km. Dashed lines indicate data window used to evaluate the autoregressive models; solid vertical line indicates automated pick; dotted vertical lines show the estimated standard deviation in the arrival time. Note the impulsiveness of the *P* wave arrival, which is typical of data used in the current analysis. The zero point of the time axis is arbitrary. (b) A plot of the Akaike Information Criterion (AIC [*Takanami and Kitagawa*, 1988]) as calculated by the autoregressive method; see text for details. The minimum in the AIC defines the *P* wave onset.

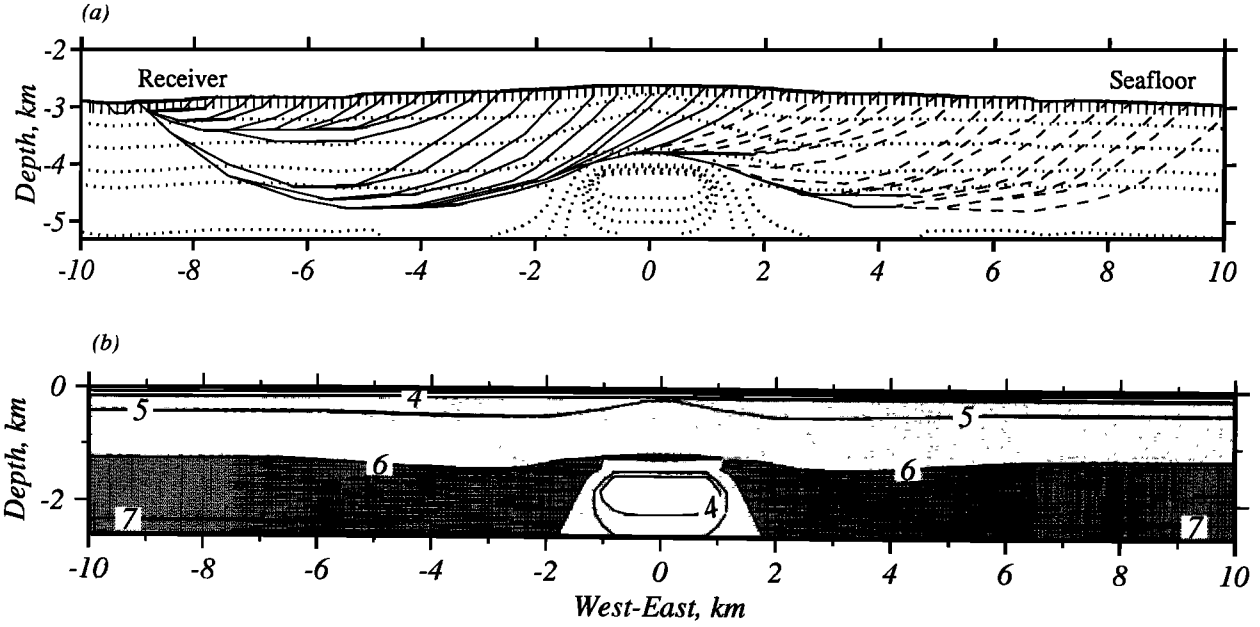

Figure 3. Seismic ray paths calculated by the shortest path method for the *P* wave velocity model of *Vera et al.* [1990]. (a) Refracted and diffracted ray paths are shown by solid and dashed lines, respectively. Data associated only with first-arriving *P* wave refractions (solid lines) are used in this study. The dotted lines indicate compressional wave velocity contours of the model shown in Figure 3b. Seafloor topography is included in the model used for seismic ray tracing; see text for details. (b) Contour plot of the two-dimensional *P* wave velocity model of *Vera et al.* [1990]; 1 km/s contour interval. Note the steep velocity gradients in the uppermost crust and near the axial magma chamber. Grey scale is as follows: 2-4 km/s (white); 4-6 km/s (light grey); 6-8 km/s (dark grey).

rameters; extending this cross section in a third dimension to define a 20 x 20 x 5 km^3 model increases the number of parameters to more than 250,000.

For seismic models similar to that of Figure 3, *Wilcock et al.* [1993b] show that many first-arriving *P* waves that propagate near the axial low-velocity volume are either strongly refracted or diffracted arrivals and that the geometry of first-arriving ray paths varies considerably with small changes in source and receiver positions. In view of the strong dependence of wave paths on the velocity model and the path endpoints, tomographic inversions must be based on an initial model that is an accurate portrayal of the known or expected heterogeneity. Additionally, the seismic ray-tracing algorithm must be capable of calculating paths and travel times through strongly heterogeneous media.

A difficulty with the seismic tomographic inverse problem, particularly when applied to areas of active magmatism, is that the number of parameters (10^5) needed to parameterize accurately a realistic model may often exceed the number of seismic delay times (~10^3-10^4) comprising a typical tomographic data set. When the dimensions of the model space exceed that of the data space, the method of regularization plays a prominent role in the form of the final solution. In the following two sections we discuss our approach to the forward problem of seismic ray tracing and to the solution of the underconstrained inverse problem.

Forward Problem

The forward problem in seismic tomography is posed as a two-point ray-tracing problem in an arbitrary medium. A solution yields a path between a source and a receiver that is an extremum with respect to travel time. Typically, the solution to be sought is the global minimum in travel time, but secondary arrivals are sometimes utilized. Because tomographic methods rely on thousands of ray paths to sample a study volume, the forward problem must be computationally efficient. To attain efficiency, several previous tomographic algorithms either sacrificed accuracy in the calculation of ray paths and travel times [e.g., *Thurber*, 1983; *Um and Thurber*, 1987] or relied on the assumption that the ray paths calculated for a one-dimensional model adequately represented those in a two- or three-dimensional structure [e.g., *Caress et al.*, 1992]. Recent advances in numerical methods, however, provide several new and more accurate approaches to calculating seismic ray paths and travel times for three-dimensional models [*Vidale*, 1990; *Moser*, 1991].

Following *Moser* [1991], we adopt the shortest path technique to solve the two-point ray tracing problem for a three-dimensional medium. The shortest path problem is well established in graph or network theory, and it has received considerable attention over several decades [e.g., *Dijkstra*, 1959]. A three-dimensional nodal representation of seismic structure is a graph, and a network suitable for travel time calculations is obtained by assigning the travel time between nodes to the arcs connecting the graph. Solving the shortest path problem for this network is equivalent to solving the forward problem of seismic tomography for first-arriving body wave energy. With the exceptions noted below, we follow *Moser's* [1991] implementation of the *Dijkstra* [1959] algorithm.

A distinct advantage of the shortest path technique is the

straightforward parameterization of complex models, including realistic seafloor topography. A model is defined by assigning slowness values at nodal points distributed throughout a volume. The nodal spacing is arbitrary, though it is frequently chosen to be identical in all coordinates. The density of nodes affects the fidelity of the velocity model, defined by the spatial limits of structural features that can be accurately portrayed [*Toomey and Foulger*, 1989] and the accuracy of the ray tracing [*Moser*, 1991]. For the steep vertical and lateral velocity gradients that typify mid-ocean ridge structure, a nodal spacing of the order of hundreds of meters or less is necessary (Figure 3). Seafloor topography is explicitly included in the model and the calculations by shearing vertically the columns of nodes to follow local seafloor relief.

An important feature of Dijkstra's algorithm is that a single solution yields the shortest path from the starting position to all nodes within the graph. Because of reciprocity of travel times with respect to the ray endpoints and because marine studies use a small number of receivers compared with sources, it is computationally efficient to consider a seafloor receiver as the starting point for seismic ray tracing. The combination of this feature of the shortest path method with a model parameterization that includes seafloor topography makes accurate water path corrections an easy task. Given the travel time field from a receiver to all nodal points on the seafloor, the minimum time path between a source in the water column and a seafloor receiver is found by searching over all possible paths connecting the two endpoints. By Fermat's principle, the path with the least time approximates the seismic ray path and yields the approximate travel time.

Inverse Problem

We have adopted a hypothesis-testing approach [e.g., *Jackson*, 1979; *Tarantola and Valette*, 1982] to the seismic tomography problem. In practice, this means that the inversion method requires the user to define a prior state of information by choosing subjectively the values of several parameters (e.g., the scale of horizontal and vertical smoothing) and the uncertainty in the prior model. The prior state of information may also include a specific hypothesis, such as two dimensionality. We consider our tomographic method as more of an adaptive inverse modeling tool than a black-box inversion method. We adopt this approach for several reasons. Foremost among these is the argument that if the number of model parameters is likely to exceed the number of independent data by several orders of magnitude, then the questions of model uniqueness and resolution in the formal sense are less important. Instead, we opt to use the tomographic method to evaluate critically specific hypotheses or to obtain a preferred image by adaptive inverse modeling. The power of this formulation is in its ability to provide the user with a tomographic tool with which to evaluate systematically one-, two-, or three-dimensional structures. The following discussion focuses on the features which distinguish our algorithm from methods currently in practice: (1) the parameterization of the inverse problem, (2) the definition of the regularizing constraints, and (3) the optimum normalization of these constraints.

The forward and inverse problems are parameterized separately for reasons of flexibility and computational efficiency. When discussing the parameterization of the forward or inverse problem, we will refer to the slowness or the perturbational model, respectively. The travel time along a path P through a slowness model $u(\mathbf{r})$ is

$$t = \int_P u(\mathbf{r})\,ds, \tag{1}$$

where $\mathbf{r}$ is the position vector and ds is the incremental path length. A general slowness field is related to a prior model $u_o(\mathbf{r})$ by

$$u(\mathbf{r}) = u_o(\mathbf{r}) + \delta u(\mathbf{r}), \tag{2}$$

where $\delta u(\mathbf{r})$ is the perturbational model. The parameterization of the slowness fields $u(\mathbf{r})$ and $u_o(\mathbf{r})$ are the same as that utilized by the shortest-path ray-tracing method. The parameterization of the perturbational model, $\delta u(\mathbf{r})$, is defined below.

Given a small perturbation to the initial slowness model, the resulting travel time variation for the kth path is

$$\delta t_k = t_k(u+\delta u) - t_k(u) = \int_P \delta u\,ds. \tag{3}$$

In accordance with Fermat's principle the travel time is stationary with respect to $P(u)$ or $P(u+\delta u)$. Equation (3) linearly relates a variation in travel time to variations in model slowness along the ray path. The perturbational model $\delta u(\mathbf{r})$ is defined by linear interpolation [e.g., *Thurber*, 1983] between model values α_i at a set of parametric nodes (i=1,...,m):

$$\delta u(\mathbf{r};\alpha_1,\alpha_2,\ldots,\alpha_m) = \sum_i^m w_i(\mathbf{r})\,\alpha_i(\mathbf{r}). \tag{4}$$

The linear interpolation weights w_i are evaluated locally using only those parametric nodes that are immediately adjacent to the position $\mathbf{r}$. For a three-dimensional parameterization of the perturbational field the summation will occur over a total of eight nonzero terms.

The advantage of the linear parameterization of $\delta u(\mathbf{r})$ is its flexibility. The perturbational parameterization is independent of the starting model; easily defined in one-, two- or three-dimensions; continuously valued; and permissive of an irregular spacing of perturbational nodes in all directions. Moreover, the number of perturbational nodes is typically less than the number of nodes used to define $u(\mathbf{r})$, allowing a computationally tractable inversion. By separating the parameterization of $u(\mathbf{r})$ and $\delta u(\mathbf{r})$ the forward problem may be evaluated over a three-dimensional volume that includes topography and a complex prior model, while the inverse problem may be limited, if desired, to finding a one-, two- or three-dimensional perturbational field that improves the fit to the data.

A relationship between a travel time misfit and the parameters defining the perturbational model is easily found by using the variational chain rule

$$\delta t_k(\alpha_1,\alpha_2,\ldots,\alpha_m) = \sum_{i=1}^m \frac{\partial t_k}{\partial \alpha_i}\alpha_i(\mathbf{r}). \tag{5}$$

Combining (3), (4), and (5) and multiplying both sides by the Kronecker delta δ_{ni} yields an expression for the travel time derivative with respect to an individual parametric nodal value used to define the perturbational model:

$$\frac{\partial t_k}{\partial \alpha_n} = \int_P w_n\,ds. \tag{6}$$

The partial derivative of a travel time with respect to a model parameter is the length of the path influenced by parameter α_n and weighted by the linear interpolation coefficient. Together, equations (5) and (6) define a set of linear equations mapping model perturbations into travel time delays.

For a set of travel time delays, equation (5) in matrix notation is familiar as

$$\mathbf{d} = \mathbf{G}\,\mathbf{m}, \tag{7}$$

where $\mathbf{d}$ is an n x 1 vector of travel time delays, $\mathbf{m}$ is an m x 1 vector whose elements are the perturbational model parameters α_i, and $\mathbf{G}$ is the Frechet matrix of partial derivatives obtained from (6). Equation (7) is ill-conditioned, making a standard least squares solution inapplicable. The inverse problem is stabilized by applying additional constraints [e.g., *Tikhonov and Arsenin*, 1977; *Jackson*, 1979; *Tarantola and Valette*, 1982], including penalties on the Euclidean size and roughness of the model vector $\mathbf{m}$. The functional we choose to minimize is

$$s^2 = \mathbf{d}^{\mathrm{T}}\mathbf{C}_d^{-1}\mathbf{d} + \lambda_p \mathbf{m}^{\mathrm{T}}\mathbf{C}_p^{-1}\mathbf{m} + \lambda_v \mathbf{m}^{\mathrm{T}}\mathbf{C}_v^{-1}\mathbf{m} + \lambda_h(\mathbf{r})\mathbf{m}^{\mathrm{T}}\mathbf{C}_h^{-1}\mathbf{m} \tag{8}$$

where λ_p, λ_v, and $\lambda_h(\mathbf{r})$ allow weighting of the importance of individual constraints, $\mathbf{C}_d$ is the data covariance matrix, and $\mathbf{C}_p$, $\mathbf{C}_v$, and $\mathbf{C}_h$ are model covariance matrices, discussed further below. The four terms on the right-hand side of (8) are the prediction error, a penalty function applied to the perturbational model, and vertical and horizontal roughening operators, respectively, also applied to the perturbational model. The weighting function for the horizontal smoothing constraint, $\lambda_h(\mathbf{r})$, is a function of position, allowing the influence of the constraint to vary throughout the model. The minimum for (8) depends on the form of the covariance matrices and the relative importance given to each of the four terms.

The data covariance matrix $\mathbf{C}_d$ describes the prior uncertainty in the travel time observations. Since the travel time observations are assumed to be independent, $\mathbf{C}_d$ is a diagonal matrix whose elements are each an estimate of the variance in an arrival time observation as calculated by the automated picking routine.

The penalty function in (8) provides a means of enforcing prior knowledge [*Menke*, 1984]. Examples of prior knowledge include a starting model defined by the results of previous experiments or inferences regarding the relative uncertainty in individual model parameters. The penalty matrix $\mathbf{C}_p$ is a diagonal matrix of the form

$$\mathbf{C}_p = \begin{bmatrix} {}_m\sigma_1^2\,{}_o u_1^2 & 0 & \cdots & 0 \\ 0 & {}_m\sigma_2^2\,{}_o u_2^2 & & \vdots \\ \vdots & & \ddots & 0 \\ 0 & \cdots & 0 & {}_m\sigma_m^2\,{}_o u_m^2 \end{bmatrix}, \tag{9}$$

where ${}_m\sigma_i$ is the prior fractional uncertainty in the ith model parameter and ${}_o u_i$ indicates the value of the prior model $u_o(\mathbf{r})$ at the position of the ith parameter. Normalization of the penalty constraint by the prior model is important for crustal studies because of the large variation in slowness with depth. In contrast, an unnormalized penalty constraint will preferentially attempt to distribute the slowness perturbations evenly throughout the model [*Wiggins*, 1972]. Because of the inverse relationship between seismic velocity and slowness, an even distribution of slowness perturbations will bias the final velocity model towards one that is characterized by increased levels of heterogeneity at greater crustal depths. The reverse is true for a tomographic algorithm that is parameterized in terms of velocity.

Spatial smoothing constraints further stabilize an inversion and allow a systematic search for the best fitting model as a function of smoothing length. Because of the strong variability of crustal slowness with depth, particularly with respect to expected lateral variations, the vertical and horizontal smoothing constraints are applied separately and each is normalized by the prior slowness model; other techniques typically use an unnormalized smoothing constraint [*Caress et al.*, 1992; *Lees and Crosson*, 1989; *White*, 1989]. Instead of attempting to calculate the inverse of the smoothing matrices $\mathbf{C}_v$ and $\mathbf{C}_h$, the smoothing constraints are applied as additional equations in the inverse problem. A smoothing constraint for the ith perturbational model parameter m_i takes the form

$$m_i\;{}_o u_i^{-1} = \frac{\sum_{j=1}^{m} \beta_j\, m_j\;{}_o u_j^{-1}}{\sum_{j=1}^{m} \beta_j}, \quad i \neq j \tag{10}$$

where the weights β_j decrease with distance from the ith model parameter. The distribution function for the weights in (10) is a Gaussian of the form

$$\beta_j = \exp\left\{ -\frac{(x_j - x_i)^2}{\tau_x^2} - \frac{(y_j - y_i)^2}{\tau_y^2} - \frac{(z_j - z_i)^2}{\tau_z^2} \right\}, \tag{11}$$

where the position of a model parameter is denoted by Cartesian coordinates x (perpendicular to the rise axis), y (parallel to the rise axis), and z (positive upward); the smoothing length is controlled by a decay parameter τ, defined separately for each coordinate direction; and only nodal positions lying within one decay length of the model parameter m_i are given nonzero weights by means of this expression. Constraints derived from (10) and (11) are applied twice to each perturbational model parameter, once each for horizontal and vertical smoothing.

Because changes in a ray path are nonlinear with respect to model perturbations, iterative methods are used to minimize (8). An inversion is initialized by choosing a starting slowness model $u_o(\mathbf{r})$ and a null perturbational model adjustment vector $\mathbf{m}_o$. After L iterations the perturbational model is the sum of all previous iterations,

$$\mathbf{m}_L = \mathbf{m}_o + \sum_{i=1}^{L} \mathbf{m}_i \tag{12}$$

and the slowness model is found from (2) and (4). A jumping strategy, as defined by *Shaw and Orcutt* [1985], is used so that the model constraints are operative on the total perturbation ($\mathbf{m}_L$) expressed with respect to the starting model ($\mathbf{m}_o$). A linear set of equations whose iterative solution satisfies (8) and incorporates the jumping strategy is

$$\begin{bmatrix} \mathbf{C}_d^{-1/2}\mathbf{G} \\ \lambda_p \mathbf{C}_p^{-1/2} \\ \lambda_v\, \mathbf{C}_v \\ \lambda_h\, \mathbf{C}_h \end{bmatrix} [\mathbf{m}_{i+1}] = \begin{bmatrix} \mathbf{C}_d^{-1/2}\mathbf{d} \\ -\lambda_p \mathbf{C}_p^{-1/2}\mathbf{m}_i \\ -\lambda_v\, \mathbf{C}_v \mathbf{m}_i \\ -\lambda_h\, \mathbf{C}_h \mathbf{m}_i \end{bmatrix}. \tag{13}$$

A single iteration consists of solving the forward ray-tracing problem; evaluating **d**, **G**, and the elements of the right-hand-side vector and left-hand-side matrix in (13); solving for a new set of model perturbations; and applying these perturbations to the slowness model. We use the LSQR method to solve (13), since this routine does not introduce bias in the presence of column rescaling or the addition of constraint equations [*Paige and Saunders*, 1982; *van der Sluis and van der Vorst*, 1987]. Iterations proceed as long as the successive reduction in the variance of travel time observations is statistically significant, as determined by an *F* test [*Thurber*, 1983].

In comparison with other tomographic algorithms [e.g., *Thurber*, 1983; *White*, 1989; *Caress et al.*, 1992; *Hole*, 1992], our inversion method incorporates a relatively large number of user-defined variables. Because of the importance of the user's input and judgment to the final results, we prefer to view our method as a combined forward-inverse modeling technique. To explore the model space the user must choose iteratively values of a half dozen different inversion variables (τ_x, τ_y, τ_z, λ_p, ${}_v\lambda_s$, ${}_h\lambda_s(\mathbf{r})$) one of which is spatially variable, as well as the initial model and its associated uncertainty. The final choice of values, while guided by numerical experimentation, is necessarily subjective. This situation is not fundamentally different from other tomographic methods in which a preferred model is subjectively chosen on the basis of a trade-off curve between the rms travel time residual and the value of one, or perhaps two, Lagrangian multipliers [e.g., *Thurber*, 1983; *White*, 1989; *Caress et al.*, 1992]. What is different about our procedure is that we cannot easily define the *n*-dimensional trade-off surface that is governed by the free variables. The chosen values of the inversion variables should represent a compromise between the objectives of diminishing the prediction error and obtaining a set of results that are robust and geologically plausible. The results presented in the next section demonstrate that a judicious and geologically motivated choice of inversion parameters yields superior results in comparison with those attained from heretofore more standard approaches to the seismic tomography problem.

Results

We present the results of two- and three-dimensional tomographic inversions that test several models of shallow crustal heterogeneity. We begin with the null hypothesis that the two-dimensional rise-symmetric model of *Vera et al.* [1990] (Figure 3) fully describes the shallow crustal structure at 9°30'N; this model was constructed to match the results of seismic reflection profiling and the one-dimensional interpretation of four rise-parallel refraction lines spaced at intervals of 1-7 km. On the basis of the inversion results we reject this hypothesis and proceed to test other two-dimensional models, including ones that are symmetric and asymmetric about the rise. We find that all inversions constrained to be two-dimensional result in substantial artifacts at depths of 1.5-2.5 km beneath the rise axis. Last, we present the results of three-dimensional inversions, which demonstrate that the shallow crustal seismic structure of the EPR is laterally heterogeneous on a scale of kilometers in both the along- and cross-axis directions.

In all cases discussed below the seismic velocity model was defined in a 20 x 18 x 2.6 km^3 volume using a grid spacing of 200 m in all dimensions; there are a total of 128,674 model parameters. To depict seafloor bathymetry, a Sea Beam map of the site, gridded at 80-m intervals [*Wilcock et al.*, 1993a], was used to deform the mesh as discussed above. The data set comprised 1459 first-arriving *P* wave travel times and their associated uncertainties.

Two-Dimensional Rise-Symmetric Inversions

We begin with inversions for two-dimensional crustal structure under an imposed constraint of axial symmetry. The optimum strike of the axis of symmetry was determined by trial and error. The values of the free parameters in the inversion algorithm were determined by conducting a series of inversions using synthetic data calculated from the two-dimensional model in Figure 3 and a source and receiver geometry identical to that of the tomography experiment. Synthetic inversions were initialized by one-dimensional and two-dimensional models, and tens of synthetic runs were analyzed prior to selecting final parameters. The results of a two-dimensional synthetic inversion with the preferred values of the free parameters and under the assumption that the uncertainty in the prior slowness model is uniform are shown in Figure 4. The parameters are as follows: $\tau_x = 0.7$ km, $\tau_z = 0.3$ km, $\lambda_p = 0.01$, $\lambda_v = 100$, $\lambda_h(\mathbf{r}) = 300$ within 4.6 km of the rise; the value of $\lambda_h(\mathbf{r})$ beyond 4.6 km from the rise axis is discussed below. Note that in each dimension the width of the averaging kernel is twice the decay parameter τ. Figure 4 shows that the final parameter values allow imaging of features with minimum dimensions of 1-2 km horizontally and 0.5 km vertically.

An important result of the synthetic inversions is that a constant horizontal smoothing parameter gives rise to anomalies beneath the off-axis receivers that are not present in the synthetic model. These artifacts are a consequence of minimizing a functional that includes contributions from the perturbational model. The functional in (8) is particularly sensitive to the magnitude of the largest model perturbation, in effect biasing the results toward an even (smooth) distribution of heterogeneity. Near the axis of a mid-ocean ridge such a bias is counter to expectation. We consequently made the geologically motivated assumption that axial structure, compared with off-axis structure, is more heterogeneous. This assumption is incorporated in the inversion by increasing the off-axis value of the weighting function for horizontal smoothing, $\lambda_h(\mathbf{r})$, to 500 times the near-axis value. The location of the transition from near- to off-axis smoothing values was chosen by trial and error. A transition within 2 km of the rise resulted in artifacts (i.e., features that are not present in the known synthetic model) beneath the summit, while a transition beyond 5-6 km from the axis resulted in artifacts beneath the off-axis stations. Results without artifacts were achieved for a transition at 3-5 km from the rise axis.

Results from an inversion of the actual data from 9°30'N, under the assumption of axial symmetry and given that the starting model is that of *Vera et al.* [1990] (Figure 3b), are shown in Figure 5. The rms travel time residual was reduced from 55 to 25 ms after four iterations, a variance reduction of 79%. Figure 5 shows the following pattern of *P* wave velocity anomalies: Centered on the rise axis and within the uppermost 500 m of the crust is a volume of relatively high velocity. Compared with the off-axis crust at similar depths the velocity contrast exceeds 1 km/s; nearly half of this contrast is not present in the starting model. Beneath this axial high-velocity anomaly, and between 700 m depth and

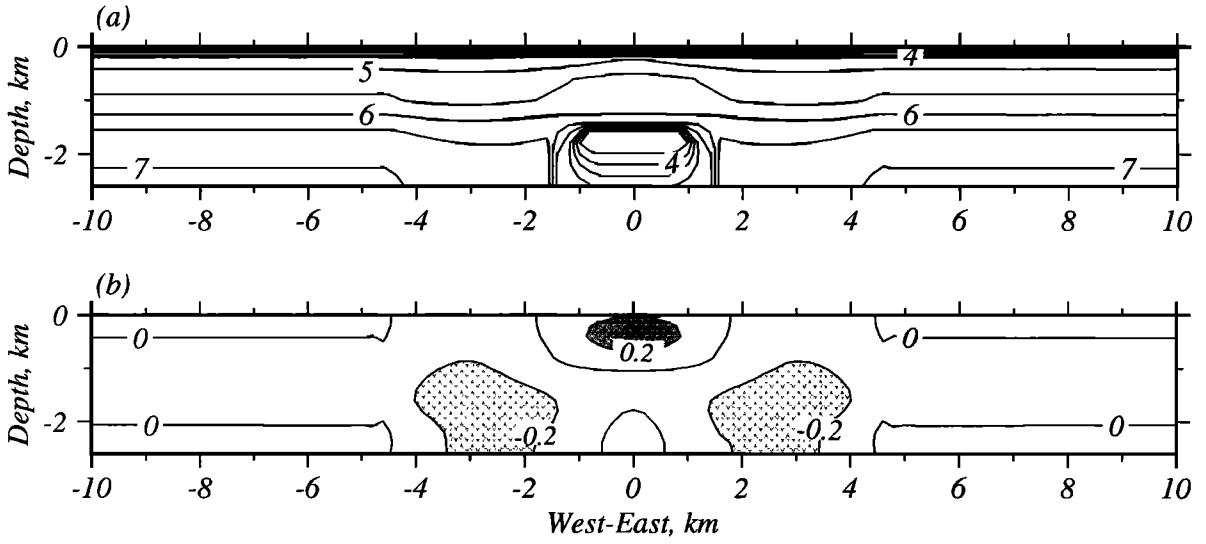

Figure 4. Results of a two-dimensional rise-symmetric inversion of synthetic data calculated from the model in Figure 3. The starting model for this inversion was similar to Figure 3b, except that the structure above 1.5 km depth was taken to be one-dimensional. (a) The final velocity model obtained from the synthetic inversion. Contour interval is 0.5 km/s. (b) Model perturbations resulting from tomographic inversion, contoured at an interval of 0.2 km/s; parts of the model with perturbations more negative than -0.2 km/s are lightly shaded; those with perturbations greater than 0.2 km/s are darkly shaded.

the top of the AMC reflector (1.6 km beneath the seafloor), lies a volume of anomalously low velocity. The lateral contrast for this anomaly is 0.2-0.4 km/s. The velocity perturbations in the shallow crust off-axis are systematically negative relative to the model of *Vera et al.* [1990], a consequence of the greater areal coverage of the tomography data in comparison with the refraction profiles; this point is discussed further below. These features were common to all inversions initialized by the model of Figure 3b.

At depths more than 1.5 km beneath the rise summit a questionable pattern of anomalous velocities was imaged in the vicinity of the axial magmatic system. Figure 5b shows a region of positive velocity perturbations at depths greater than 2 km beneath the rise summit and within ±2 km of the rise axis. The width of this high-velocity perturbational anomaly exceeds that of the low-velocity volume included in the starting model (Figure 3). Immediately outward of the high-velocity anomaly is a localized region of anomalously low seismic velocities. Because the axial magmatic system is not likely to be characterized by a progression from high to low velocity with distance from the rise axis, these features are probably artifacts, i.e., they are unlikely, on the basis of prior geological information, to represent features in Earth. Possible causes of such artifacts include bias in the starting velocity model, the assumption of symmetry about the rise, or the assumption of two dimensionality.

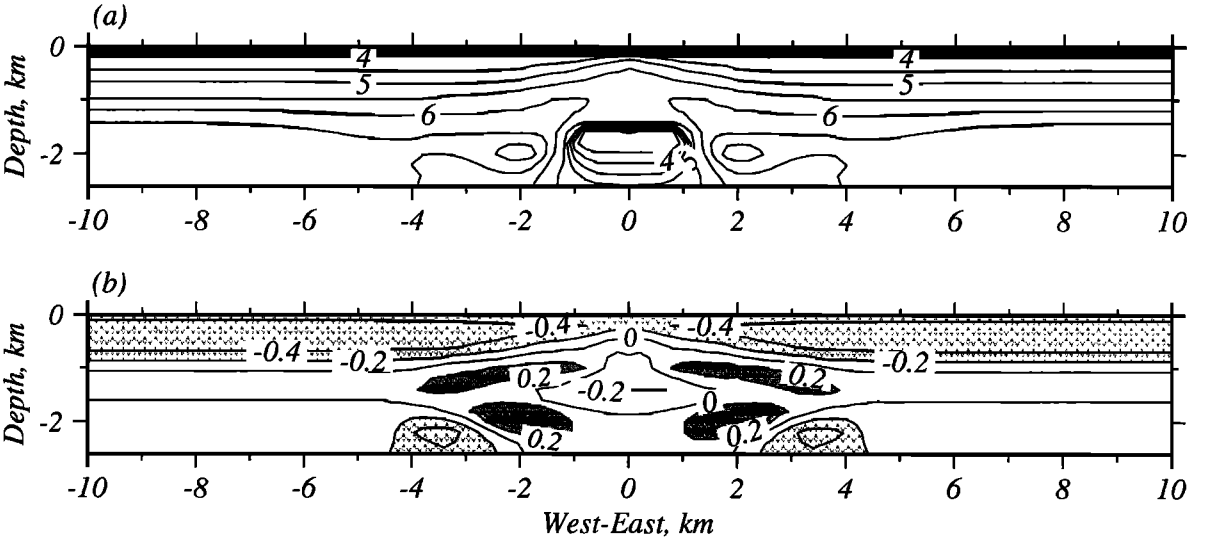

Figure 5. Results of a two-dimensional rise-symmetric inversion of data from 9°30'N; the initial model is taken from that of *Vera et al.* [1990] (Figure 3b). (a) Final velocity model obtained from the inversion. (b) Model perturbations resulting from tomographic inversion. The final model in Figure 5a is the sum of the starting model (Figure 3b) and these perturbations. Contour interval and shading are as in Figure 4.

We searched for possible adverse effects of a bias in the initial model by conducting several inversions for different end-member examples of the shallow crustal and axial magma chamber structure. Figure 6a shows a two-dimensional starting model that includes a laterally homogeneous upper crust and a midcrustal axial magma chamber anomaly. Figures 6b and 6c show the results of the inversion, which terminated after four iterations yielding an rms travel time residual of 24 ms and a variance reduction of 80%. Figure 7 shows additional results obtained for a one-dimensional starting model identical to the off-axis structure of Figure 6a. This inversion terminated after four iterations, also yielding a final rms travel time residual of 24 ms. Figures 7 and 6 demonstrate that velocity perturbations in the uppermost crust (< 1.5 km) and in the vicinity of (but not within) the axial magmatic system are similar for inversions with markedly different starting models. The imaged anomalies are thus insensitive to uncertainties in the initial model.

Two-Dimensional Asymmetric Inversions

Tomographic images obtained without imposing a symmetry constraint permit assessments of the validity of the rise-symmetry assumption and whether such a constraint is a source of artifacts. An example of such a two-dimensional asymmetric model resulting from tomographic inversion is shown in Figure 8. The *P* wave data and the values of the free parameters for this inversion are identical to those used for the symmetric models. For a starting model given by the model in Figure 6a, the inversion achieved an rms travel time residual of 20 ms and a variance reduction of 87%. An *F* test comparing the final variance in the travel time residuals for a symmetric and an asymmetric inversion (Figure 6b and 8) indicates that the improved fit attained by the asymmetric model is significant at the 95% confidence level. A comparison of Figures 8 and 6 shows that the anomalous features detected in the axial region and between the seafloor and 1.5 km depth are similar in the two models. These include the high-velocity anomaly nearest the seafloor and the low-velocity volume immediately above the AMC reflector. Figure 8 also shows a significant asymmetry in the structure of the off-axis crust at all depths. The crustal velocities to the west of the rise are 0.2-0.3 km/s less than the those to the east. The asymmetry is particularly pronounced near the seafloor and at depths of about 2 km. For reasons discussed below, however, the off-axis anomalies at depths greater than 1.5 km are likely affected by artifacts arising from the assumption of two dimensionality. Last, adjacent to the rise axis at depths greater than 1.5 km, Figure 8 again shows a suspect pattern of anomalous velocity, with high-velocity perturbations occurring near the axial magma chamber. These patterns of anomalous velocities were found to be independent of the starting model, including models with and without an axial magma chamber anomaly. We conclude from these results and those above that if the anomalies imaged near the axial magmatic system at depths greater than

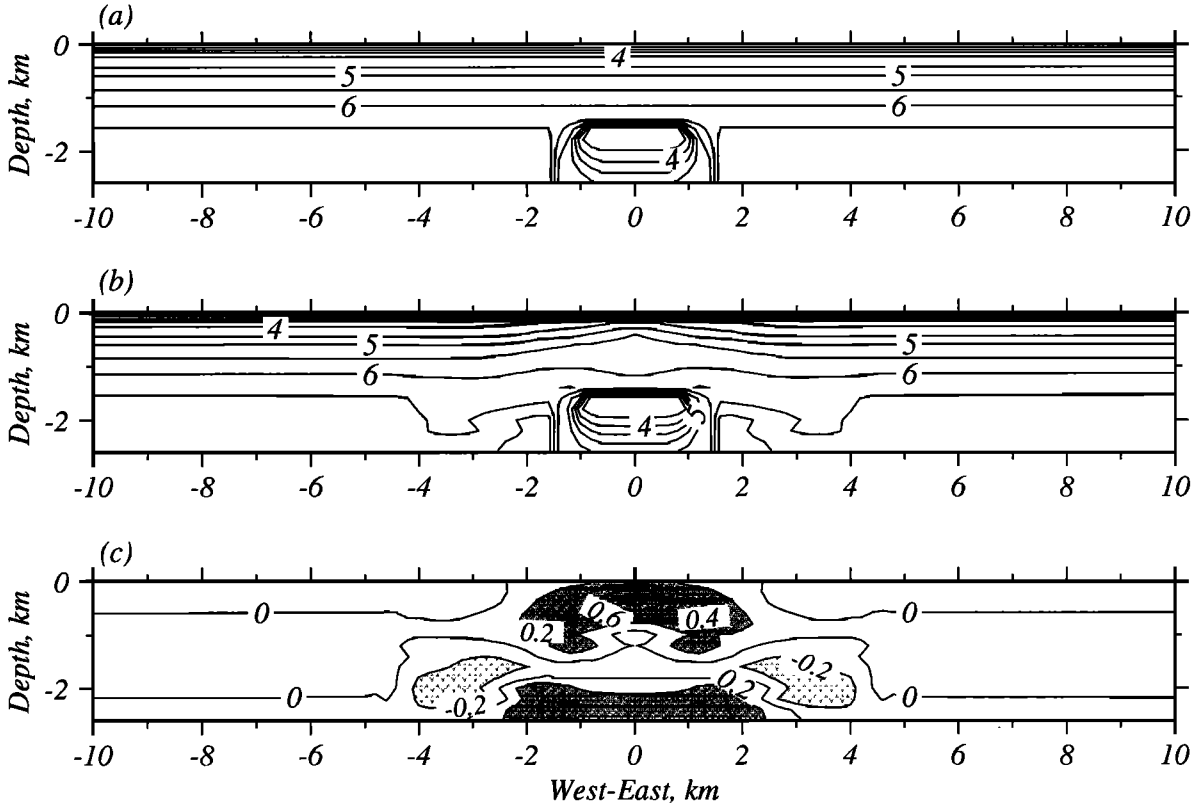

Figure 6. Results of a two-dimensional rise-symmetric inversion of data from 9°30'N; the shallow crustal structure of the initial model is identical to the off-axis structure shown in Figure 5a; the axial magma chamber anomaly at depths greater than 1.6 km is taken from Figure 3b. (a) Starting model contoured at intervals of 1 km/s. (b) Final model resulting from tomographic inversion. Note the similarities to Figure 5a. (c) Model perturbations resulting from tomographic inversion; contour interval and shading are as in Figure 4. Perturbations are greater than in Figure 5b because of the different initial models.

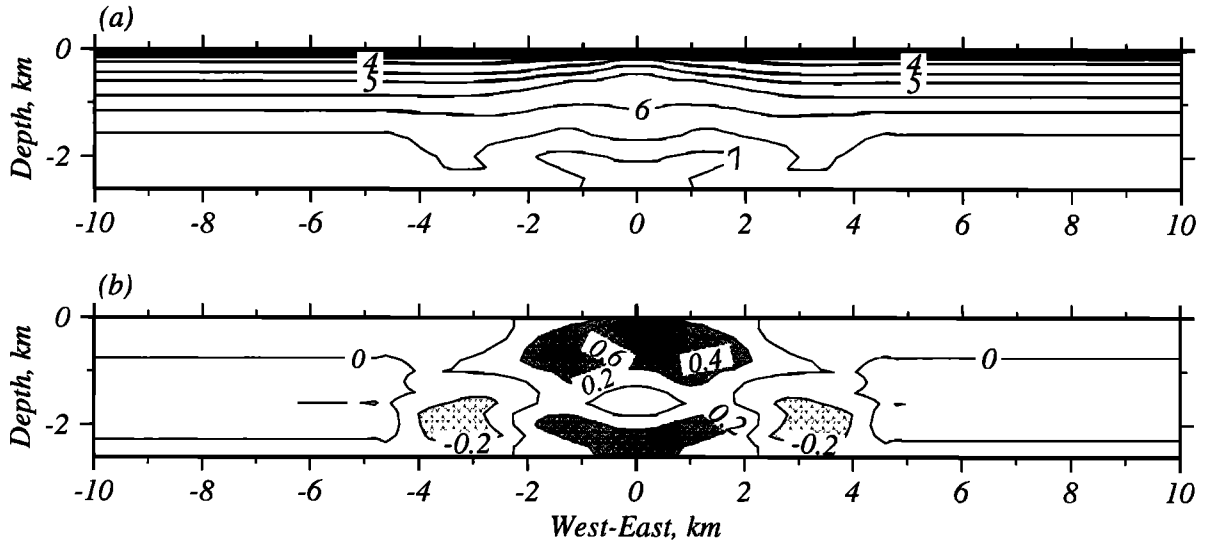

Figure 7. Results of a two-dimensional rise-symmetric inversion of data from 9°30'N; the initial model is one-dimensional. (a) Final model resulting from tomographic inversion; contour interval is 1 km/s. Note the similarities to Figures 5a and 6b. (b) Model perturbations; contour interval and shading are as in Figure 4. The results are similar to those of Figure 6c.

1.5 km are indeed artifacts, then their cause is the assumption of two dimensionality.

In summary, the results of two-dimensional inversions, including both symmetric and asymmetric models, show features at depths less than 1.5 km beneath the seafloor that are either not present or not fully developed in the model of *Vera et al.* [1990] or *Toomey et al.* [1990]. These include a more pronounced axial high-velocity anomaly near the seafloor and an off-axis structure that is asymmetric; results presented below demonstrate that these anomalies are not artifacts resulting from the assumption of two dimensionality. In both cases, the differences between our results and those of *Vera et al.* [1990] may be attributed to the more complete areal coverage of the tomography data which allows us to map structures that may be missed by rise-parallel refraction profiles spaced at intervals of kilometers. For instance, the majority of the refraction profiles of *Vera et al.* [1990] are located to the east of the rise, making it difficult to recover asymmetric structure. We have also shown that the two-dimensional images are not unduly sensitive to the assumed initial structure of the shallow crust or the presence or absence in the starting model of an axial magma chamber anomaly. Relaxation of the symmetry constraint indicates that an asymmetric model, characterized by lower seismic velocities to the west of the rise, provides an improved fit to the data. All inversions conducted under the assumption of two dimensionality,

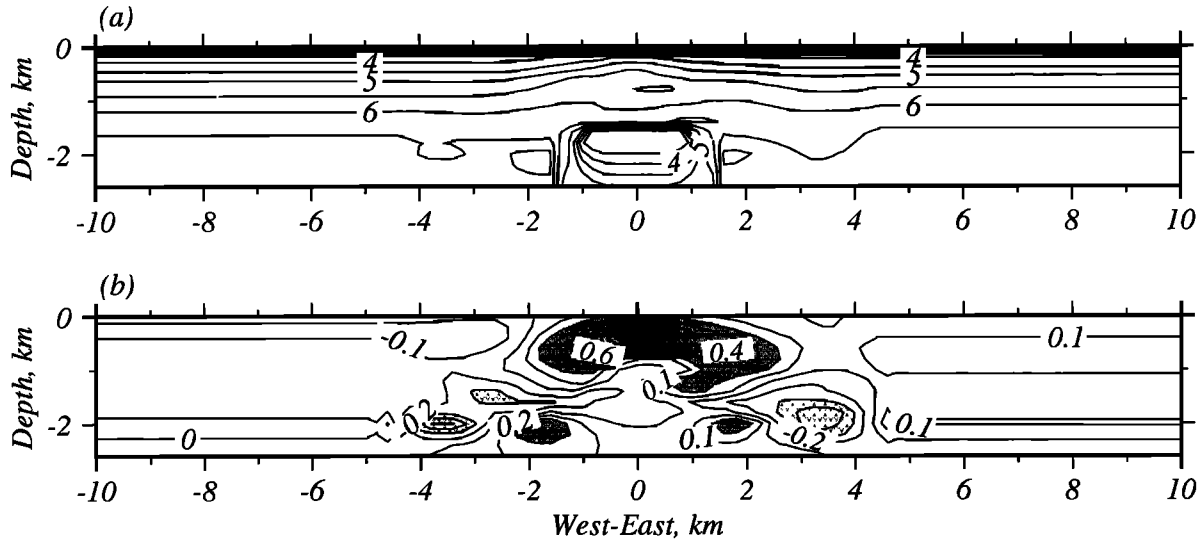

Figure 8. Results of a two-dimensional inversion without the constraint of rise symmetry. The starting model is that in Figure 6a. (a) Final asymmetric model; contour interval is 0.5 km/s. (b) Asymmetric model perturbations contoured at an interval of 0.1 km/s; shading are as in Figure 4. Note that the contour interval is different from previous figures so as to show the asymmetry in the off-axis velocity anomalies. Velocities are significantly lower to the west of the rise axis at depths less than 1 km beneath the seafloor.

however, gave rise to features in the vicinity of the axial magma chamber at depths in excess of 1.5 km that are inconsistent with geologic expectation and other seismic data.

Three-Dimensional Inversions

The presentation of the results of our three-dimensional inversions is divided into three parts: a summary of procedural details, an analysis of resolution, and a description of the three-dimensional model. An interpretation of model features follows in a subsequent section.

Description of procedure. We performed over 50 tomographic inversions to model the three-dimensional shallow crustal seismic structure. These tomographic analyses systematically evaluated the effects of varying the initial slowness model, the three-dimensional parameterization of the perturbational model, and the values of the inversion parameters. As with the two-dimensional inversions, the slowness model was parameterized throughout a 20 x 18 x 2.6 km^3 volume using a grid spacing of 200 m in all directions. We conducted inversions with both one-dimensional and two-dimensional starting models. The two-dimensional structures included models symmetric and asymmetric with respect to the rise axis, as well as models with and without an axial magma chamber anomaly. In no instance did we observe any strong sensitivity to the initial model.

For the results shown below the perturbational model was parameterized by a nodal spacing of 200 m in the vertical direction and 500 m in the cross- and along-axis directions, for a total of 21,238 perturbational parameters. The number of perturbational parameters is considerably less than the number of parameters used to define the model for ray tracing (128,674). We also used coarser parameterizations of the perturbational model in the early stages of the analyses, since they are more efficient computationally, to analyze the effects of varying the starting model and the inversion parameters. Similar results were obtained for both coarse and fine parameterizations of the perturbational model.

The inversion parameters were varied to evaluate their influence on the tomographic image. The Lagrangian multipliers λ_v and $\lambda_h(\mathbf{r})$ for the vertical and horizontal smoothing constraints varied, respectively, over the ranges 50-200 and 100-500. The horizontal decay parameters τ_x and τ_y, were varied independently from 0.7 to 2.1 km; the vertical decay parameter was held fixed at 0.3 km. The results obtained for this range of inversion parameters followed expectations, in that larger values of either the smoothing weight (λ) or length (τ) tended to mute the imaged anomalies, while smaller values gave rise to shorter-wavelength features characterized by more pronounced heterogeneity. For the results shown below, and the analysis of resolution, the values of the inversion parameters were τ_x = 1.1 km, τ_y = 2.1 km, τ_z = 0.3 km, λ_p = 0.01, λ_v = 100, and $\lambda_h(\mathbf{r})$ = 100. For this set of values the imaged anomalies are representative of those features which were common to nearly all inversions.

A stepwise inversion approach was adopted to obtain the preferred tomographic image. First, we solved for a three-dimensional model where the off-axis crustal structure was forced to be approximately one-dimensional. This assumption was imposed by increasing the off-axis value of $\lambda_h(\mathbf{r})$ to 500 times the axial value. The boundary between the different smoothing domains was placed at a distance of 4.6 km from the rise axis. The results from this inversion were then used as the starting model for a subsequent tomographic analysis where the value of $\lambda_h(\mathbf{r})$ was set to 100 throughout the model domain. The first stage of this procedure inhibits aliasing of axial anomalies to off-axis positions, while the later stage allows imaging of off-axis heterogeneity. In contrast, images obtained without employing a two-step procedure, i.e., with a spatially invariant value of $\lambda_h(\mathbf{r})$, resulted in significant artifacts beneath off-axis stations and a noticeable aliasing or streaking of axial anomalies in the off-axis directions.

The two-dimensional model shown in Figure 6a was used to initialize the stepwise inversion procedure. The structure of the starting model at depths less than 1.5 km beneath the seafloor is one-dimensional, while at depths greater than this the only cross-axis anomaly is the pronounced low-velocity feature in the vicinity of the AMC reflector. A one-dimensional model of the shallow crust was preferred for initializing the inversions since it would not bias the three-dimensional images toward a linear, two-dimensional representation of rise-parallel features. Because the ray paths used in the inversion do not penetrate the volume immediately encompassing the melt lens, its presence in the starting model has little effect on the final solution. Indeed, inversion results obtained for the midcrust with a one-dimensional starting model were similar. For the initial model in Figure 6a the rms travel time residual is 53 ms. Following the first stage of the inversion procedure, where the off-axis structure was constrained to be approximately one-dimensional, the rms travel time residual after four iterations was 14 ms. Using the final model from this inversion as the starting model for the second stage of the inversion procedure, where the off-axis smoothing constraint was relaxed, the tomographic analysis terminated after two iterations, yielding an rms travel time residual of 9 ms. Relative to the initial starting model (Figure 6a), the total variance reduction was over 95%. An *F* test comparing the final variance in the travel time residuals for the three- and two-dimensional inversions indicates that the improved fit attained by the three-dimensional model is significant at the 95% confidence level.

The results of three-dimensional tomographic imaging are presented in Plate 1, which shows map view sections through the tomographic image at depth intervals of 200 m. The maps in Plate 1 depict anomalous velocities, contoured at intervals of 0.2 km/s, relative to the starting model shown in Figure 6a. Because the starting model includes the axial magma chamber anomaly, the contour maps do not include this feature at depths greater than 1.6 km. The final velocity model is a sum of the starting model (Figure 6a) and the model perturbations in Plate 1. The depths of these map view sections are defined relative to the seafloor topography, rather than a flat-lying datum. Thus each section is a surface that is conformable to the seafloor. The seafloor bathymetry in the area of the tomographic imaging is shown in Figure 9.

Resolution analysis. The resolution of the three-dimensional tomographic images is evaluated by empirical methods that include examination of the distribution of seismic ray paths and the results of synthetic inversion for known structures. A measure of the distribution of seismic ray paths near the *i*th model parameter, the derivative weight sum (DWS) [*Thurber*, 1983; *Toomey and Foulger*, 1989], is obtained from equation (6) as

$$\mathrm{DWS}(\alpha_i) = \sum_{k=1}^{n} \frac{\partial t_k}{\partial \alpha_i}, \tag{14}$$

where the summation is over all possible seismic ray paths.

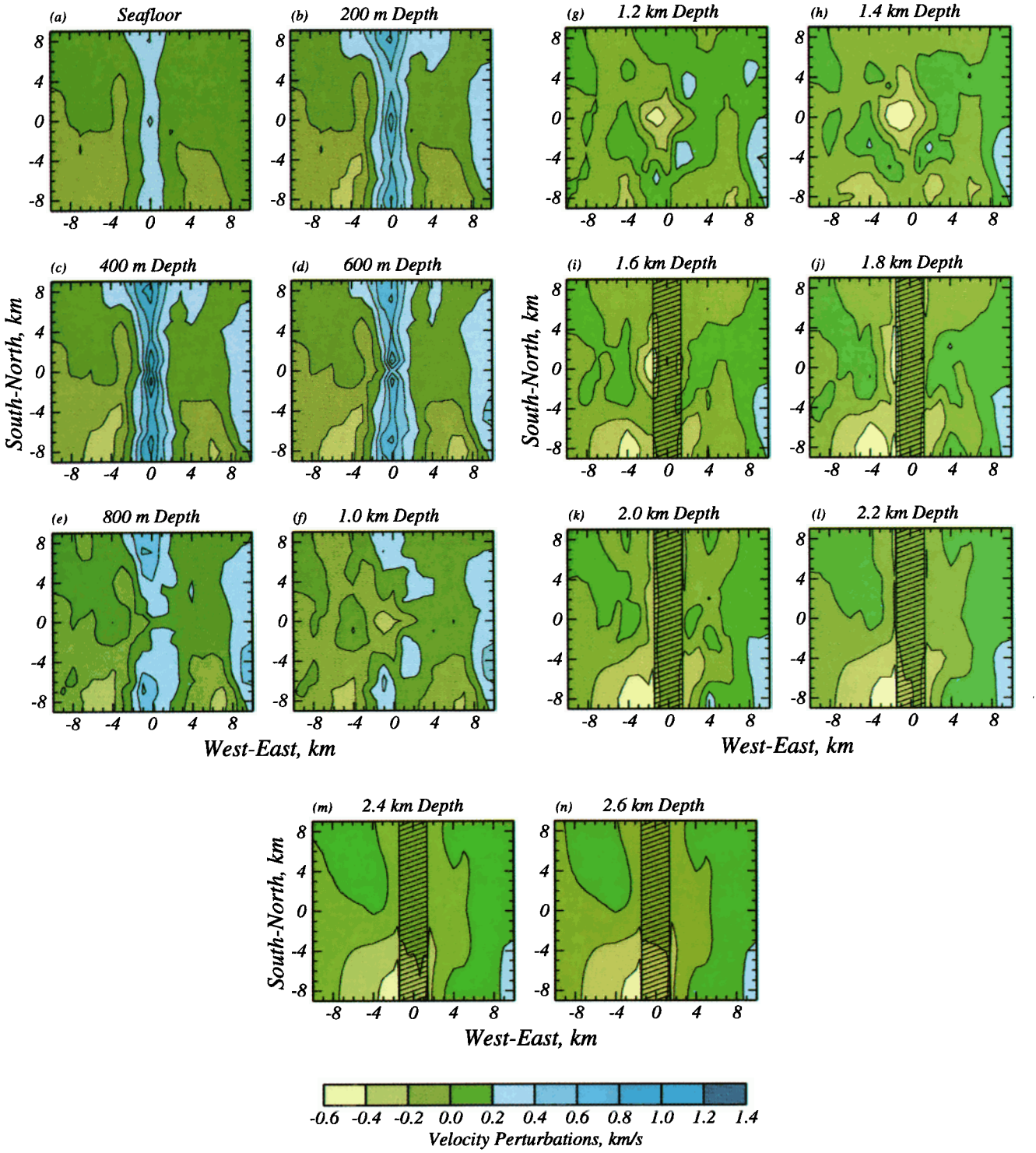

Plate 1. Results of a three-dimensional inversion; the initial model is the two-dimensional starting model shown in Figure 6a. (a)-(n) Map view sections of the anomalous velocity perturbations relative to the prior model. Sections are shown at 200-m intervals from the seafloor down to 2.6 km depth. Except for the hachured region, the velocity of the prior model at the depth of each section is as follows: (a) 1.9 km/s, (b) 3.9 km/s, (c) 4.4 km/s, (d) 5.0 km/s, (e) 5.4 km/s, (f) 5.7 km/s, (g) 6.1 km/s, (h) 6.4 km/s, (i) 6.5 km/s, (j) 6.7 km/s, (k)-(n) 6.8 km/s. The contour interval is 0.2 km/s. Hachured area at depths of 1.6-2.6 km delimits its approximate location of axial magma chamber anomaly included in the starting model. See text for discussion.

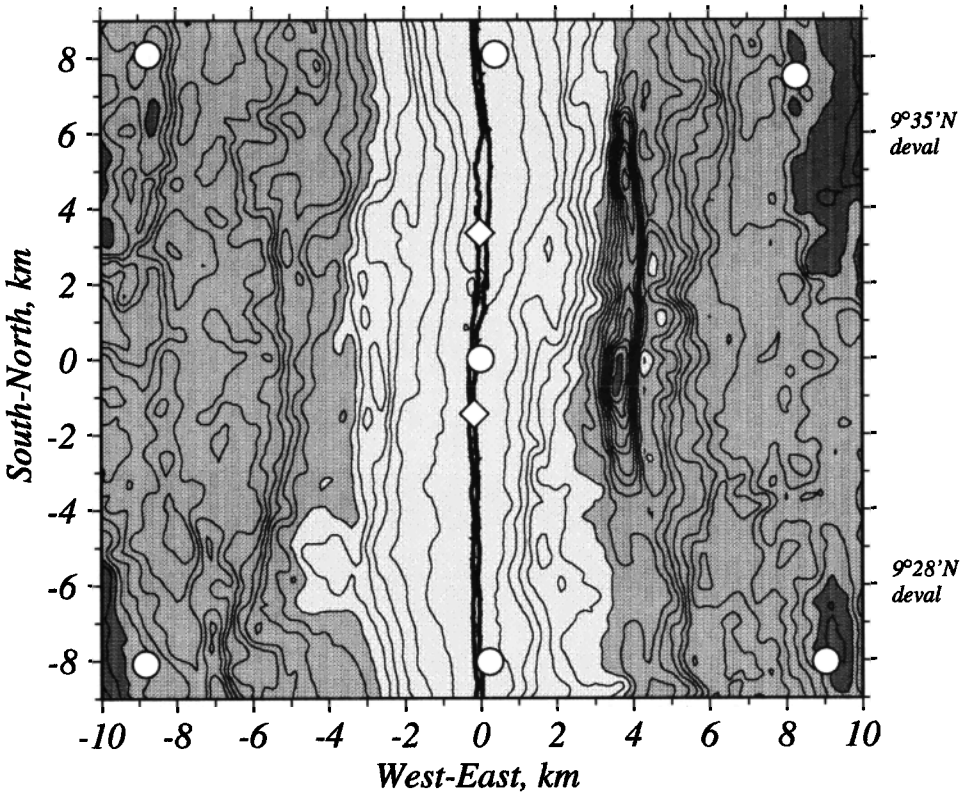

Figure 9. Seafloor bathymetry within the region of tomographic imaging. The axes coincide with those of Plate 1. The contour interval is 20 m, and the shading is identical to that of Figure 1. Open circles denote ocean bottom receiver locations. Heavy lines along the rise axis delimit the axial summit caldera, and open diamonds indicate known sites of high-temperature hydrothermal activity [*Haymon et al.*, 1991].

The DWS is a weighted sum of the path lengths influenced by a model parameter. Because (14) is sensitive to the spatial separation between a ray path and a node via the weighting function in (6), it provides a measure of seismic ray path distribution that is superior to an unweighted count of the rays that sample a model parameter.

Contour maps of the spatially averaged DWS determined from three-dimensional paths calculated for the final tomographic image are shown at several depths in Figure 10; the averaging is defined by the smoothing constraints expressed in (10) and (11). As expected the DWS is typically greater beneath seismic stations, particularly near the seafloor. Because most ray paths penetrate the upper few hundred meters of oceanic crust at near vertical angles, the shallow crustal DWS is low in areas removed from a station. At depths of 400-600 m the DWS exceeds 0.25 km throughout most of model and at depths of 0.8-1.2 km the DWS, on average, exceeds 0.5 km; beneath the rise axis the average DWS values exceed 0.5 km at depths as shallow as 400 m. We can thus expect that the resolution of shallow crustal structure will be better beneath the rise axis than in off-axis areas distant from a receiver. At depths of 1.2-1.6 km the DWS values generally increase throughout the model space, indicating that sampling at these depths is distributed more evenly. The general increase in DWS at depths of 1-2 km is a result of rays that turn at these depths and thus travel horizontally for a significant distance. The absence of ray paths through the axial low-velocity anomaly at depths greater than 1.6 km beneath the rise axis is apparent as near-zero values of the DWS. However, off axis the DWS values deeper than 1.6 km are generally higher and more evenly distributed than at shallower depths. From these results we can infer that the resolution of seismic structure should increase with depth in our models and that the poorest resolved regions will be the shallowmost crust away from the rise and distant from a station. This latter inference is understood as the effect of a lack of turning rays within the upper few hundred meters of off-axis oceanic crust. In contrast, the presence of three on-axis stations ensures that the shallowmost axial crust will be sampled by turning rays.

A common practice for evaluating the resolution of a tomographic image is to reconstruct a known pattern of anomalies [e.g., *Humphreys and Clayton*, 1990] using a ray set calculated for the final tomographic model. We conducted inversions for several synthetic models characterized by homogeneous blocks, 2 km on a side and with a velocity of 6.0 km/s, imbedded in material with a velocity of 5.0 km/s; each block was 400 m in thickness. We conducted inversions for each of several different depths to the top of the blocks (200 m, 800 m, and 1.4 km). Each synthetic inversion used a ray set defined for the model in Plate 1; no iterations were permitted in these synthetic reconstructions.

The results of these synthetic experiments indicate that model resolution is best at depths of 1-2 km. At these depths the reconstruction of synthetic anomalies was particularly good, with vertical and lateral streaking of no more than a few hundred meters; streaking within a few hundred meters of the blocks is expected because of the length scale of smoothing. These results are consistent with the high levels of the DWS at

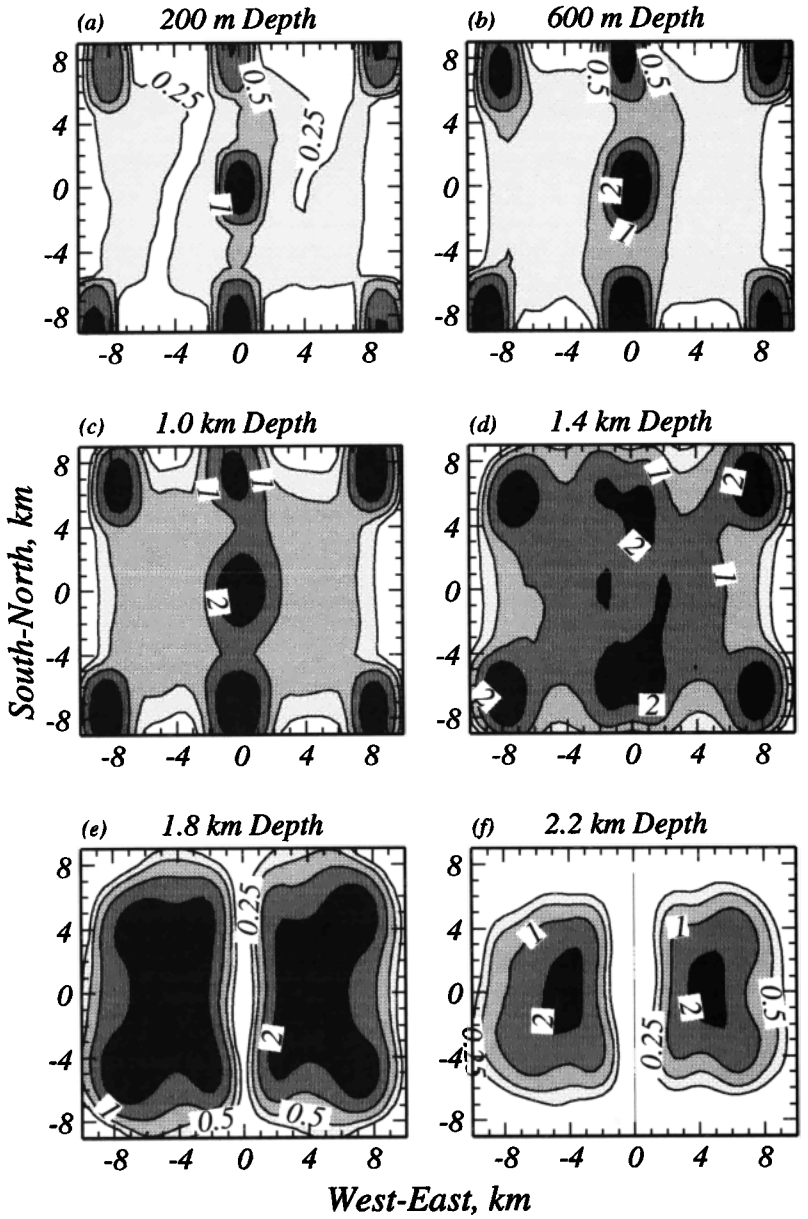

Figure 10. Map view sections of the derivative weight sum (DWS). The DWS is contoured at values of 0.25, 0.5, 1.0, and 2.0 km. See text for discussion.

depths of 1-2 km beneath the seafloor. At depths less than 1 km beneath the seafloor the ability to reconstruct the lateral dimensions of an anomaly was good, but the synthetic reconstructions showed significant upward streaking, particularly at off-axis sites and above the anomalous bodies. At shallow depths the upward streaking is a consequence of the predominance of vertical ray paths within the upper kilometer of the crust. The results of inversion for blocks within a kilometer of the seafloor were consistent with the DWS values in that the reconstruction of the anomalies was best beneath the rise axis.

Features of the model. An inspection of the contour maps in Plate 1 shows the following features. Between the seafloor and a depth of 800 m beneath the seafloor, the rise axis is characterized by anomalously high velocities. A comparison of the sections in this depth range shows that the near-seafloor axial high-velocity anomaly is most pronounced at depths of 400-600 m, where the lateral velocity contrast across the rise approaches 1 km/s. Along the rise at these depths the velocity varies by 0.4 km/s, and the overall width of the high-velocity anomaly is greatest near 9°35'N (y = 6 km) and 9°28'N (y = -6 km). The cross-axis component of this feature has been imaged previously in this area by several studies, including tomographic imaging [*Toomey et al.*, 1990], on-bottom seismic refraction [*Christeson et al.*, 1992], and multichannel seismic reflection experiments [*Harding et al.*, 1993]. In addition, seismic studies of the EPR at other sites have yielded a similar cross-axis result [e.g., *McClain et al.*, 1985; *Caress et al.*, 1992].

Beneath the rise summit, at depths of 1-1.6 km, the tomographic images (Plates 1f-1i) show a volume of anomalously low velocity which is restricted along the rise to -4 km < y < 4 km. The depth extent of this low-velocity feature places it above the AMC reflector at 1.6±0.1 km depth [*Detrick et al.*, 1987; *Vera et al.*, 1990; *Kent et al.*, 1990, 1993; *Harding et*

al., 1993]. Within the aperture of the tomography experiment the along-axis variation in the depth of the reflector, probably less than 100 m [*Harding et al.*, 1993], is considerably smaller than the thickness of the low-velocity volume present in the tomographic images, indicating that this feature is not the result of depth variations in the melt lens. At depths of 1-1.4 km the region of lowest velocities is offset to the west of the rise axis, similar to the westward offset of the low-velocity volume imaged previously by *Toomey et al.* [1990] at depths of 2-3 km. An inspection of the anomalous velocity map at a depth of 1.2 km shows that the magnitude of the velocity contrast across and along axis is more than 0.4 km/s over distances of 2-3 km. Because the data used in the current analysis come from paths that do not penetrate the melt lens as constrained by MCS data [*Detrick et al.*, 1987; *Kent et al.*, 1990, 1993], the tomographic image in Plate 1 does not resolve anomalous features directly beneath the rise summit at depths greater than 1.6 km. However, in combination with our earlier results, we can conclude that the low-velocity anomaly imaged above 1.6 km depth in Plate 1, or above the AMC reflector, is an upward continuation of a previously imaged midcrustal (2-3 km depth) low-velocity anomaly [*Toomey et al.*, 1990].

Toward the south of the imaged volume a broad low-velocity anomaly is apparent at depths near the AMC reflector (~1.6 km). Given the axial magma chamber anomaly in the starting model (Figure 6a), inspection of the map view sections at 1.4-2 km depth in Plate 1 shows that the low-velocity volume south of 9°28'N broadens to a width of over 5-7 km at depths of only 1.6-2 km. To the west of the rise axis this anomaly is particularly pronounced from the uppermost crust down to approximately 2 km depth, although the magnitude of the anomaly varies with depth. A similar broadening of the low-velocity anomaly near 2 km depth was observed in our earlier tomographic images [*Toomey et al.*, 1990, Figure 3].

Away from the EPR summit the crustal structure is heterogeneous and asymmetric with respect to the rise axis. Map view sections at depths of 400 and 600 m (Plate 1) show that the average shallow crustal velocity is higher to the north and east than it is to the south and west, an observation consistent with the results of *Harding et al.* [1993] and *Christeson* [1994]. Within the region of the image the lowest velocities in the shallow crust are located beneath the western flanks of the rise summit south of 9°28'N. From the resolution analysis we can conclude that such lateral variation in the shallow crustal structure is resolved; however, the anomalies will be aliased toward the seafloor, resulting in seafloor velocities that are slightly less than values typically reported (~2 km/s) [*Christeson et al.*, 1992; *Harding et al.*, 1993; *Vera and Diebold*, 1994; *Vera et al.*, 1990]. Furthermore, the resolution analysis indicates that these lateral variations are averages over depth intervals of several hundred meters at a depth where seismic layer 2A is observed to vary considerably in total thickness both near- and off-axis [*Christeson et al.*, 1992; *Harding et al.*, 1993; *Vera and Diebold*, 1994]. Because the seismic velocities of layer 2B are generally greater than that of layer 2A, a thickening of layer 2A would appear as a shallow low-velocity feature in our tomographic maps, a point discussed further below. The east-west asymmetry observed in the shallow crust persists at depths of 1.6-2.6 km, where crustal velocities to the west are lower by as much as 0.2-0.3 km/s.

Vertical sections through the tomographic image are shown in Plates 2 and 3. Plate 2 shows the anomalous velocity, relative to the two-dimensional starting model (Figure 6a), for cross-axis sections at $y = \pm 6$ km and ± 1 km. Comparison of these sections shows that the along-axis structure of the shallow crust is markedly variable, with much of the variability characterized by differences in the cross-axis width of the near-seafloor axial high-velocity anomaly and location and form of the low-velocity anomaly that lies beneath this surficial anomaly and above the melt lens at 1.6 km depth. The widening of the near-seafloor high-velocity anomaly near 9°28'N and 9°35'N (±6 km) is apparent. Also evident in the southernmost cross section is the volume of low velocities approximately 4 km west of the rise summit. This anomaly extends from near the seafloor to a depth of at least 2 km. Last, a comparison of the off-axis structure for all three cross sections shows that the seismic velocities are systematically lower on the western flank of the rise.

Rise-parallel vertical sections of the anomalous structure, relative to the two-dimensional starting model, are shown in Plate 3. The sections 1 km to either side of the rise summit show that the low-velocity anomaly at depths of 1-1.5 km is most pronounced midway between 9°28'N and 9°35'N and offset to the west of the rise axis. A comparison of the shallow axial section with those 1 km to either side provides another illustration that the high-velocity anomaly near the seafloor is wider to the north and south than near the center of the section.

A comparison of our current results with those previously reported [*Toomey et al.*, 1990], which were obtained with a different tomographic algorithm [*Thurber*, 1983] and a different subset of the overall data set, indicates that our new analysis provides an improved fit to the data and images of anomalous features that were formerly undetected. Previously, we were able to reduce the weighted rms travel time residuals to 42 ms, in comparison with the rms of 9 ms reported here. We attribute this improvement, in part, to a more accurate ray-tracing algorithm and to an inversion approach that permits simultaneously a densely parameterized slowness model and a well-conditioned search for a smooth perturbational model. Indeed, despite increasing the density of the perturbational model by 4-5 times that previously used, we obtained an image that is visibly smoother and presumably less influenced by ill-conditioning. Perhaps more importantly, the new images show features not fully present in our previous report, such as the off-axis asymmetry in the shallow crust, the along-axis variation in uppermost axial crustal structure, and the horizontal and vertical dimensions of the low-velocity volume overlying the AMC reflector.

Interpretation and Discussion

The three-dimensional tomographic images of the crustal structure immediately above the AMC reflector are characterized by two anomalous features that vary systematically along the rise axis: A volume of anomalously low velocity extending 300-500 m above the AMC reflector and a region of anomalously high velocity within 1 km of the seafloor. The along-axis length scales for both of these velocity anomalies are similar to those of other seafloor features. In the area of our experiment, two discontinuities in the local trend of the axial high, known as deviations from axial linearity, or devals [*Langmuir et al.*, 1986], occur near 9°28'N and 9°35'N (Figure 9). Devals occur at approximately 10-km intervals along this

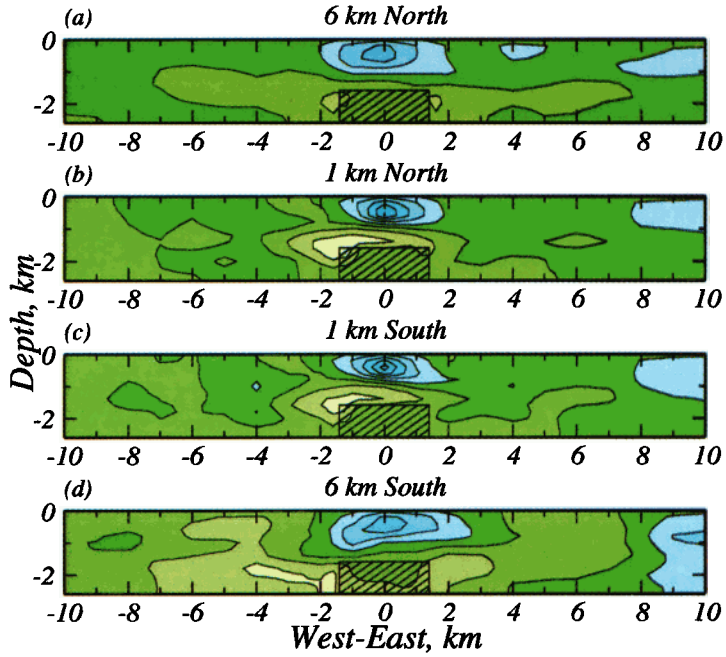

Plate 2. Rise-perpendicular vertical sections through the three-dimensional tomographic image showing the anomalous velocity perturbations relative to the starting model (Figure 6a). The location of the sections can be determined from Figure 9. Contour interval and color scale are the same as in Plate 1; hachured area shows location of axial magma chamber anomaly included in the starting model.

portion of the EPR [*Langmuir et al.*, 1986; *Haymon et al.*, 1991; *Wilcock et al.*, 1993a] and define the smallest scale of segmentation of the rise axis [*Macdonald et al.*, 1988]. Devals are often accompanied by offsets in the axial summit caldera (ASC), a linear feature identified from side scan sonar images and inferred to be the result of collapse following magma withdrawal [*Haymon et al.*, 1991]. Video imagery and submersible observations along the rise axis near 9°30'N have

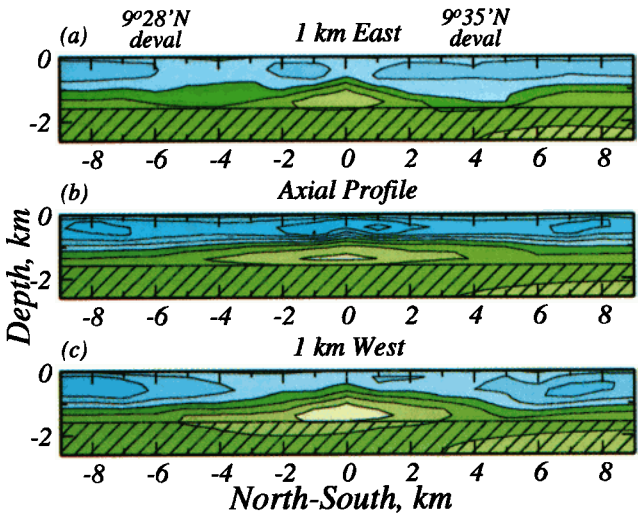

Plate 3. Rise-parallel vertical sections through the three-dimensional tomographic image showing the anomalous velocity perturbations relative to the starting model (Figure 6a). The location of the sections can be determined from Figure 9. Contour interval and color scale are the same as in Plate 1; hachured area shows location of axial magma chamber anomaly included in the starting model.

been used to show that changes in the characteristics of the ASC and in the distribution of black-smoker hydrothermal vents occur between deval-bounded rise segments [*Haymon et al.*, 1991]. The similarity in the along-axis scales of seafloor morphologic features, the distribution of hydrothermal vents (Figure 9), and the underlying seismic velocity structure (Plates 1-3) has important implications for axial processes.

Between the two devals at 9°28'N and 9°35'N, anomalously low velocities extend upward from the AMC reflector at 1.6 km depth [*Detrick et al.*, 1987; *Vera et al.*, 1990; *Kent et al.*, 1990, 1993] to approximately 1 km beneath the seafloor. By the usual lithologic interpretation of the distribution of seismic velocity with depth in oceanic crust, this low-velocity anomaly occurs within the sheeted dike complex inferred to lie immediately above the melt lens [*Vera et al.*, 1990; *Kent et al.*, 1993; *Harding et al.*, 1993]. At these depths beneath the rise summit the imaged seismic velocities are lowest midway between the devals. The along-axis heterogeneity exceeds 0.5 km/s; the cross-axis velocity perturbation is approximately 0.2-0.5 km/s. The offset of the low-velocity anomaly to the west of the rise axis is similar to the offset of both the AMC reflector at this site [*Detrick et al.*, 1987; *Kent et al.*, 1993a; *Mutter et al.*, 1988] and the low-velocity volume previously imaged by *Toomey et al.* [1990] at depths of 2-3 km. Along-axis variations in the midcrustal low-velocity volume were previously interpreted as evidence for segmentation of the crustal thermal structure. Similarly, we interpret the region of lowered velocities above the AMC reflector as an upward continuation of the segmented thermal anomaly that envelops the axial magmatic system. Further evidence for a low-velocity anomaly immediately above the AMC reflector was reported by *Vera et al.* [1990] from a one-dimensional analysis of rise-parallel refraction lines. Their results showed that *P* wave velocities above the AMC reflector decreased with depth from 6.25 to 4.5 km/s over a 300-m depth interval, while *S*

wave velocities stayed relatively constant. The marked decrease in *P* wave velocities, without a similar decrease in *S* wave velocities, is most likely the result of a subsolidus thermal anomaly in the crust above the melt lens [*Vera et al.*, 1990; *Toomey et al.*, 1990]. A porosity-induced velocity anomaly would reduce both *P* and *S* wave velocities [*Berge et al.*, 1992], contradicting the observations of *Vera et al.* [1990].

We thus infer that the tomographically imaged low-velocity volume above the AMC reflector is the result of anomalously high, but subsolidus, temperatures within the sheeted dike complex. The velocity contrast of 0.2-0.5 km/s across the rise, by this view, implies a cross-axis thermal anomaly of at least 250°-450°C [*Christensen*, 1979]. A thermal anomaly in excess of about 400°C may be indicative of rock not presently experiencing penetrative cooling by hydrothermal fluids [e.g., *Lowell*, 1991]. Because tomographic imaging usually underestimates the magnitude of a low-velocity anomaly [*Hole*, 1992], we conducted several inversions to test if our data were consistent with the results of *Vera et al.* [1990] that showed *P* wave velocities decreasing by 1.75 km/s within 300 m depth of the AMC reflector. For starting models that included either a negative or zero velocity gradient with depth above the AMC reflector the perturbational models obtained by tomographic inversion were nearly identical. From this result we conclude that the tomographic solutions are insensitive to the precise form of the velocity-depth gradient just above the AMC reflector. However, the tomographic analysis does require a rise-parallel velocity heterogeneity within the sheeted dikes immediately above the AMC reflector of at least 0.5 km/s (Plates 1f-1h). Along-axis variations in seismic structure at this depth imply attendant along-axis thermal gradients within the sheeted dike complex. The sites of active high-temperature vents mapped by *Haymon et al.* [1991] in our experiment area (y = +3, -1 in Figure 9) correlate well with the locus of lowest axial velocities and inferred greatest temperatures at 1.2-1.6 km depth (Plates 1h-1j). This correlation suggests that the inferred thermal gradient affects the present geometry of hydrothermal circulation and favors the focusing of upwelling fluids above regions of highest temperature.

Further evidence for segmentation of the seismic velocity structure, and by inference the crustal thermal structure, is a broad low-velocity anomaly imaged south of the 9°28'N deval at depths near the AMC reflector (~1.6 km) (Plates 1i-1k and 2d). The cross-axis width of this anomaly, which includes the low-velocity magma chamber anomaly in the starting model (Figure 6) and regions where velocities are anomalously low by more than 0.2 km/s, is 8-10 km at depths of 1.6 to 2 km (Plates 1i-1k). The low-velocity anomaly is not symmetric about the rise; it is particularly pronounced to the west of the rise axis where it is at least 2 km thick. This anomaly also lies beneath a bathymetric feature 60 m in height that may be a volcanic edifice (Figure 9) and near to where *Mutter et al.* [1988] and *Kent et al.* [1993] observe the AMC reflector to the west of the rise summit. The rise flank east and south of 9°28'N is underlain by a smaller volume of moderately low seismic velocities at depths of 1 to 2.5 km (Plate 2d). Our previous tomographic images had also shown that the low-velocity anomaly at 2 km depth [*Toomey et al.*, 1990, Figure 3] broadened to the south of 9°28'N. We attribute the broad low-velocity anomaly south of the 9°28'N deval to elevated temperatures. The magnitude of the velocity anomaly, by this interpretation, requires an off-axis thermal anomaly of 300-500°C.

The low-velocity anomaly south of the 9°28'N deval is associated with an apparent increase in the width of the rise summit (Figure 9). For example, the 11-km width of the 2750-m contour at 9°28'N is the largest in the area of tomographic imaging, and it exceeds by 3 km the width of the same contour level at 9°35'N. These observations suggest that the width of the axial summit may correlate with the width of the low-velocity volume that envelops the axial magmatic system. In addition, these limited observations suggest that the segmentation of the rise axis morphology, as defined by seafloor devals, is similar to that of the underlying seismic crustal structure. We speculate from these observations that the emplacement of magma within the upper crust occurs over a wider cross-axial region in the vicinity of the 9°28'N deval. From the present images we cannot ascertain if the increased width of the emplacement zone is the result of a broader region of magma ascent within the crust [*Kent et al.*, 1993] or, alternatively, the effect of offsets in the along-axis loci of migration of comparatively narrow magmatic injection zones [*Batiza and Margolis*, 1986; *Langmuir et al.*, 1986; *Macdonald et al.*, 1988].

A high-velocity anomaly centered on the rise axis and restricted to lie between the seafloor and 800 m depth provides improved constraints on the processes of formation of shallow oceanic crust and further evidence for a relationship between segmentation of seafloor features and seismic crustal structure. This near-seafloor high-velocity anomaly was also detected in our earlier tomographic images and was attributed to a sheeted dike complex at shallower than normal depths beneath the neovolcanic zone [*Toomey et al.*, 1990]. The feature is better resolved by the new imaging techniques developed in this study. Several recent investigations have successfully yielded images of the seismic boundary separating the extrusive layer from the underlying dikes [*Christeson et al.*, 1992; *Harding et al.*, 1993] and have generally confirmed our interpretation. In particular, *Harding et al.* [1993] conclude from an analysis of multichannel seismic profiling data that seismic layer 2A, generally thought to consist of volcanic material, thickens from 200 m to 400 m within 1-2 km of the rise axis. This near-axis variation in shallow structure is likely a result of repeated eruptions at axial vents of lava that flow outward from the eruption site, giving rise to a progressive thickening of the volcanic section (seismic layer 2A) with age [*Toomey et al.*, 1990; *Harding et al.* 1993]. Because tomographic methods are sensitive to the bulk seismic velocity averaged over scales of hundreds of meters, an off-axis thickening of the volcanic carapace (layer 2A) appears as a shallow low-velocity feature in our tomographic maps. While other factors such as fault-related porosity or hydrothermal alteration undoubtedly affect bulk seismic structure [e.g., *Wilcock et al.*, 1992b], the correspondence between our results and those of *Harding et al.* [1993] suggests that a variation in the thickness of layer 2A, interpreted as the extrusive layer, is the dominant cause of variations in upper crustal velocity. We suggest that a low- or high-velocity anomaly within 600 m of the seafloor is generally indicative of a thick or thin extrusive section, respectively.

A comparison of the seafloor morphology and the location of the ASC [*Haymon et al.*, 1991] (Figure 9) with the tomographic images shows that the axial high-velocity anomaly is narrowest at a point on the axis midway between the 9°28'N

and 9°35'N devals. North of the 9°35'N deval the tips of the en echelon segments of the ASC overlap [*Haymon et al.*, 1991, Figure 4], and just south of 9°35'N the ASC changes in strike and width (Figure 9). These surficial changes in the ASC coincide with an increase in the width of the high-velocity anomaly. The broadening of the high-velocity anomaly near 9°35'N and the coincident overlap of en echelon segments of the ASC [*Haymon et al.*, 1991] are consistent with an overall increase in the width of the dike injection zone beneath the northern deval. A similar increase in the width of the high-velocity anomaly near 9°28'N, where the axial summit caldera is poorly defined [*Haymon et al.*, 1991, Table 2], suggests that an increase in the width of the dike injection zone beneath seafloor devals may be a common phenomenon. Alternatively, these results may indicate a decrease in the thickness of the extrusives due to a decrease in the eruptive flux near devals.

Our preferred interpretation of the segmentation of the seismic velocity structure of the shallow axial crust is that it arises from the interaction of individual elongate axial volcanoes [e.g., *Langmuir et al.*, 1986; *Batiza and Margolis*, 1986; *Macdonald et al.*, 1988; *Toomey et al.*, 1990]. By this view, the aperture of our experiment includes a 12-km-long axial volcano, its bounding devals, and portions of the adjacent volcanic segments. At 9°30'N the 12-km-long volcanic segment is characterized near its center by anomalously low velocities at depths of 1-3 km (this paper and *Toomey et al.* [1990]), a pattern that is consistent with a segmented thermal structure and the injection of mantle-derived melt midway along the segment. The distal ends of this inferred volcanic segment are accompanied by a widening of the near-seafloor high-velocity anomaly, which we interpret as evidence for en echelon overlap of the dike injection zone of adjacent axial volcanoes. The relationship between segmentation of seismic velocity structure in the upper 3 km of crust (*Toomey et al.* [1990] and this paper) to the seismic structure of the lower crust and upper mantle is not yet well constrained. Thus it is not known if there is a magmatic segmentation in the lowermost crust and uppermost mantle or, if so, whether its scale is similar to that of the inferred volcanic segmentation of the rise axis upper crust.

The seismic observations from 9°30'N constrain the physical structure of the boundary separating the high-temperature magma reservoir from the lower-temperature regime dominated by hydrothermal circulation. As noted above, the tomographic solutions, in conjunction with the results of *Vera et al.* [1990], suggest that the AMC reflector at 9°30'N [*Detrick et al.*, 1987; *Kent et al.*, 1990, 1993] is overlain by a thermal anomaly approximately 300-500 m in thickness. This interpretation has several implications for the recent evolution of both the crustal thermal structure and the depth of penetration of hydrothermal fluids above the melt lens. Approximating the inferred thermal anomaly as a rectangle of cross-sectional area 1 km wide by 500 m high with an average temperature contrast of 350°C relative to the surroundings, the excess heat content per meter of rise axis is approximately 6×10^{11} kJ (for a density of 2900 kg m^{-3} and a specific heat of 1.2 kJ kg^{-1} K^{-1}). In comparison, a 3-m-wide dike injected into the same 500-m-high region delivers 9×10^9 kJ of heat per meter of rise axis (for an initial temperature of 1300°C and a latent heat of fusion of 400 kJ kg^{-1}). If all dike-generated heat remains in the system, to accumulate the heat within the region above the AMC would require nearly 70 dike injection episodes, or 2×10^3 years at a full spreading rate of 110 mm y^{-1}. Alternatively, a thermal anomaly above a midcrustal melt lens may result from purely conductive heating, giving rise to a thermal boundary layer that separates the hydrothermal and magmatic regimes. For the instantaneous heating of a half-space, a time interval of $1\text{-}2 \times 10^3$ years would be necessary to develop a 300- to 500-m-thick thermal anomaly above a melt lens if no boundary layer were present prior to cooling (for a thermal diffusivity of 1 mm^2 s^{-1}). Thus the estimated time interval required to establish the inferred thermal anomaly is comparable for purely conductive and advective heat transport. In a more realistic system, both modes of heat transfer would occur, and they would be accompanied by hydrothermal circulation. Under the assumption that heat loss out of the system is the dominant term among those not included, these simple calculations provide a lower bound estimate of 10^3 years since the 300- to 500-m-thick region immediately above the melt lens has undergone penetrative cooling by hydrothermal fluids.

The lack of symmetry of shallow crustal structure about the rise axis suggests that off-axis magmatism is an important process along this section of the EPR. Throughout the experiment area, the shallow crustal seismic velocities are generally greater to the north and east. Under the premise that velocity anomalies within approximately 600 m of the seafloor are a result of variations in the thickness of the volcanic section, the tomographic results suggest that this extrusive layer thickens from north to south and from east to west. In support of this interpretation, *Christeson* [1994] reports that the thickness of layer 2A 5 to 8 km west of the rise increases southward from 310 m to 580 m between 9°30'N and 9°27'N, respectively, and *Harding et al.* [1993] report a similar cross-axis asymmetry in the thickness of layer 2A. Since it is unlikely that the cross-axis asymmetry in the thickness of the volcanic section could result from strictly axial processes, we interpret these results as evidence for increased off-axis volcanism toward the southwestern quadrant of our experiment area. This interpretation is in agreement with multichannel seismic reflection data that show a westward displacement of the AMC reflector from the rise summit in the southern half of our experiment site [*Mutter et al.*, 1988; *Kent et al.*, 1993] and recent submersible and geochemical studies that indicate that off-axis volcanism is more prevalent to the west than to the east [*Fornari et al.*, 1992; *Perfit et al.*, 1992, 1994; *Goldstein et al.*, 1994]. Further evidence for off-axis volcanism is the bathymetric high west of the 9°28'N deval that is inferred to be a volcanic edifice. The particularly low seismic velocity of the shallow crust beneath this feature may indicate an anomalously thick pile of volcanic material or, perhaps, a shallow crustal thermal anomaly.

The east-west asymmetry in the off-axis seismic structure at depths of 1-2.4 km suggests that crustal temperatures, on average, are also asymmetric about the rise axis. To the west of the rise the average seismic velocities are 0.2-0.3 km/s lower than those to the east. Under the assumption that the seismic anomaly is the result of elevated temperatures, the crust to the west is at least ~100°C hotter. Higher crustal temperatures to the west of the rise may result from cross-axis variations in either off-axis magmatism or the efficiency of hydrothermal cooling. The former interpretation would be consistent with the inferred increase in the thickness of the volcanic units to the west of the rise axis.

Conclusions

We have presented a new method for seismic tomography using delay times of first-arriving *P* waves and applied the method to a subset of high-quality data collected on the East Pacific Rise near 9°30'N. Our tomographic method provides several new methodological advances that improve the accuracy of the solutions to both the forward and inverse problems. The forward problem includes realistic representation of seafloor topography, a model parameterization that accurately reproduces the strong vertical and lateral gradients that typify oceanic crustal structure, and accurate three-dimensional ray tracing using the shortest path method [*Moser*, 1991]. Our formulation of the inverse problem allows modeling of one-, two-, and three-dimensional structures, and it includes an unbiased normalization of prior constraints and a formalism that permits hypothesis testing. In comparison with our previous results [*Toomey et al.*, 1990] the new method yields an improved fit to the data and better resolution of three-dimensional crustal structure.

Our tomographic analysis has focused on the two- and three-dimensional structure of the crust immediately above the axial magma chamber and the off-axis structure above 2.5 km depth. From the results of tomographic imaging, we rejected the hypotheses that the shallow crustal structure is two-dimensional and demonstrated that inversions conducted under the assumption of two-dimensionality gave rise to significant artifacts. The three-dimensional tomographic images show anomalous features that correlate with variations in the axial and off-axis seafloor morphology, the location and form of the axial summit caldera, and the distribution of high-temperature hydrothermal activity.

The three-dimensional structure of the shallow crust beneath the summit of the EPR is characterized by two anomalous features segmented along the rise on a scale similar to that of the axial morphology and the axial summit caldera. The first feature is a high-velocity anomaly that occurs within 800 m of the seafloor and 1-2 km of the rise axis. This anomaly was previously reported by *Toomey et al.* [1990], but it is better resolved in the current tomographic images. We attribute this high-velocity anomaly to the presence of sheeted dikes at shallower than normal depths beneath the neovolcanic zone, an interpretation supported by several other seismic studies [*Christeson et al.*, 1992; *Harding et al.*, 1993]; with increasing age the dikes are progressively buried lava flows from near axis vents. The new images presented here show further that the high-velocity anomaly broadens beneath two seafloor morphologic discontinuities, or devals. We interpret this broadening as evidence for an increase in the width of dike injection beneath devals due to en echelon overlap of adjacent volcanic segments.

The second feature imaged beneath the rise summit is a volume of anomalously low velocities extending upward from the depth of the AMC reflector (1.6 km) to approximately 1 km beneath the seafloor. This low-velocity anomaly, up to 2 km in half width, is most pronounced midway between the seafloor devals, and its segmentation is similar to that of the low-velocity volume imaged at depths of 2-3 km [*Toomey et al.*, 1990, Figure 3]. We attribute this low-velocity anomaly to elevated temperatures within the sheeted dike complex that overlies the AMC reflector. The segmentation of the inferred thermal anomaly is consistent with the hypothesis that mantle-derived melt is injected midway along a locally linear segment of the rise bounded by seafloor devals. By this view the observed segmentation of the crustal seismic structure is a result of segmentation of the rise into elongate axial volcanoes with a rise-parallel dimension of approximately 10 km [*Langmuir et al.*, 1986; *Batiza and Margolis*, 1986; *Macdonald et al.*, 1988; *Toomey et al.*, 1990].

Seismic observations at 9°30'N indicate that the AMC reflector at 1.6 km depth [*Detrick et al.*, 1987; *Kent et al.* 1990, 1993] is overlain by a seismic velocity anomaly 300-500 m in thickness [*Vera et al.*, 1990, *Toomey et al.*, 1990; this paper]. Provided that this seismic anomaly is due solely to temperature, the tomographically imaged low-velocity anomaly requires a thermal anomaly of 250°-450°C. The tomographic data are also consistent with a larger velocity reduction, as reported by *Vera et al.* [1990], and by inference a larger temperature anomaly above the AMC reflector. On the basis of this interpretation it was estimated that a 300- to 500-m-thick region immediately above the midcrustal melt lens has not undergone penetrative cooling by hydrothermal fluids in the last 10^3 years.

Away from the EPR summit the crustal structure is laterally heterogeneous and asymmetric with respect to the rise axis. Within 600 m of the seafloor the average shallow crustal velocity is higher to the north and east than to the south and west. The lowest velocities in the shallow crust are located immediately beneath an inferred volcanic edifice west of the rise summit. An east-west asymmetry is also observed in the structure at 1-2 km depth, with crustal velocities to the west of the rise generally lower by 0.1-0.2 km/s. On the basis of these observations we infer that off-axis magmatism along this section of the EPR affects the thickness of the volcanic section and perhaps the thermal structure of young oceanic crust. In particular, the variations in structure within 600 m of the seafloor support the view that off-axis volcanism has increased the thickness of layer 2A in the south and west of the study area, an interpretation also supported by the results of *Harding et al.* [1993] and *Christeson* [1994]. The lower velocities observed to the west of the rise at 1-2 km depth are attributed to elevated temperatures resulting from either increased off-axis magmatism or a decrease in the efficiency of hydrothermal cooling.

Appendix: Instrument and Source Relocation

To estimate receiver and source positions, we used a method similar to that of *Creager and Dorman* [1982] . This technique uses water wave arrival times from shots deployed during periods of Global Positioning System (GPS) coverage to fix simultaneously the locations of the seafloor receivers and the source parameters. The estimation of receiver and source parameters was a two-stage process. First, from the arrival times of the water waves for a subset of 20% of the shots, source parameters and positions of the 15 ocean bottom receivers were estimated simultaneously. Second, from the receiver positions so relocated, we calculated source parameters for all shots from water wave arrival times.

To determine the range of reliable water path data, we examined the travel time curves for each instrument. For the AOBH and DOBH receivers, water wave arrivals were easily identified to ranges of 20 km or more on a channel recording high-pass-filtered (0.15-2 kHz) and rectified energy [*Koelsch and Purdy*, 1979; *Koelsch et al.*, 1982]. In contrast, for the OBSs, which record water wave data on the seismometer channels, the

acoustic arrival at ranges greater than 14-17 km was difficult to identify, probably because the dominant frequency of the energy was greater than the 60-Hz upper limit of the instrument passband [*Mattaboni and Solomon*, 1977]. Further evidence for this inference is that on the lower-frequency data channel (1-60 Hz) of the hydrophone instruments the water wave arrival was also difficult to identify beyond 15 km range. For the 13 hydrophone instruments the maximum range of reliable data was taken to be 20 km. For the two OBSs the maximum range of a direct arrival was a function of receiver depth; the off- and on-axis instrument yielded reliable data to ranges of 16 and 14.5 km, respectively.

The relocation procedure requires a velocity-depth profile in the water column. At depths greater than 100 m beneath sea level the sound speed is well known. Our estimate of the speed of sound in the upper 100 m was derived from an expendable bathythermograph profile taken in the vicinity of the seismic experiment and the assumption of a uniform layer above the source position. The velocity in this layer was determined from the inversion results, as described below.

Initial estimates of shot positions and instrument depths and the observed water wave arrival times are inputs to the inversion algorithm. All data are accompanied by prior uncertainties which are used to weight the least squares inversion. Initial shot locations were taken to be the GPS-navigated position at the time the shot was launched from the research vessel. Because of the likelihood of drift between the time of deployment and detonation, the standard deviation in a shot position was assumed to be 500 m. Estimates of the receiver depths were taken from the bathymetric depth at the time of deployment as derived from Sea Beam. While Sea Beam is generally accurate to within 10 m over smooth terrain, because of the possible nonvertical free-fall of the deployed packages the prior standard deviation in instrument depth was assumed to be 25 m. Given these prior uncertainties in shot positions and instrument depths, the principal inversion constraints come from the water wave arrival times.

A total of 846 observations (649 arrival times, 91 initial shot locations, and 15 instrument depths) were inverted for 318 parameters (the final map positions and origin times of 91 shots and the final locations, including depth, of 15 instruments). The shots selected for the first stage of the inversion procedure provide good azimuthal coverage of each receiver position. In accordance with the method of *Creager and Dorman* [1982], we iteratively adjusted the prior uncertainty in arrival time data until the least squares estimate of χ^2 approximated the total number of degrees of freedom (528). This iterative search for the prior arrival time uncertainty that correctly scales the χ^2 statistic serves two purposes, if the uncertainties follow a Gaussian distribution. First, when the estimate of χ^2 approximates the number of degrees of freedom the a posteriori estimate of model uncertainty is scaled correctly. Second, provided that the estimates of uncertainty in all other data (shot positions and instrument depths) are valid, the value of the prior arrival time uncertainty that yields a correct scaling provides an objective estimate of the true standard deviation. Examination of the χ^2 values for a series of inversions indicated that the standard deviation in water wave arrival time is 5 ms. Test inversions were also conducted to explore the effects of the assumed velocity within the homogeneous surficial layer. For values between 1.530 and 1.545 km/s, the analysis of variance indicated a minimum misfit at a velocity of 1.541 km/s. Variations in final receiver positions with changes in the assumed velocity model were typically less than the a posteriori estimate of the standard deviation in receiver parameters. Table 1 lists the final instrument locations and their uncertainties, for values of 5 ms for the prior travel time uncertainty and 1.541 km/s for the surficial velocity. The final depth and uncertainty for the instruments was taken from the Sea Beam data [*Wilcock et al.*, 1993a].

The estimation of source parameters (latitude, longitude, and origin time) for all suitable shots, given the relocated receiver positions, is a straightforward event-location problem. Only water wave data were used in the inversion for source parameters because of their small uncertainties. We did not use estimates of either the source position at the time of deployment or the origin time as recorded by a ship-towed hydrophone to constrain final source parameters because of the likelihood of introducing bias from the drift of the charge with the prevailing currents. By limiting the available data to arrival time observations, the estimation of source parameters was restricted to only those events recorded by three or more instruments. For these 452 shots the total number of observations per event ranged from 3 to 11. Following the inversion for source parameters the rms travel time residual for shots located by four or more arrivals (420 events) was less than 10 ms in all but two instances, for which the rms travel time residual slightly exceeded 10 ms. In analyses of the distribution of travel time residuals by range, by station, by shot, and by total number of receiving stations, the final travel time residuals were well behaved, indicating no apparent source of bias. The mean and standard deviation of the water wave travel time residuals by station were in all cases effectively zero and 6 ms, respectively.

Acknowledgments. We thank the officers and crew of the R/V *Thomas Washington* and members of the scientific party for their assistance. We also thank T. Moser and A. Farley for helpful discussions concerning seismic ray tracing and graph theory and G. Barth, J. Hole, and N. Sleep for constructive and thoughtful reviews that improved the manuscript. E. Humphreys and W. Wilcock provided many encouraging and insightful comments while this work was in progress. The original data collection was supported by the National Science Foundation under grants OCE-8615797 and OCE-8615892. This analysis was supported by the Office of Naval Research under grant N00014-91-J-1216 and the National Science Foundation under grants OCE-9000177 and OCE-9106233. W.H.O.I. contribution 8685.

References

Batiza, R., and S. H. Margolis, Small non-overlapping offsets of the East Pacific Rise, *Nature, 320*, 439 -441, 1986.

Berge, P. A., G. J. Fryer, and R. H. Wilkens, Velocity-porosity relationships in the upper oceanic crust: Theoretical considerations, *J. Geophys. Res., 97*, 15,239-15,254, 1992.

Caress, D. W., M. S. Burnett, and J. A. Orcutt, Tomographic image of the axial low-velocity zone at 12°50'N on the East Pacific Rise, *J. Geophys. Res., 97*, 9243-9264, 1992.

Christensen, N. I., Compressional wave velocities in rocks at high temperatures and pressures, critical thermal gradients, and crustal low-velocity zones, *J. Geophys. Res., 84*, 6849-6857, 1979.

Christeson, G. L., Seismic constraints on shallow crustal processes at the East Pacific Rise, Ph.D. thesis, 182 pp., WHOI/MIT Joint Program in Oceanography, Woods Hole, Mass., 1994.

Christeson, G. L., G. M. Purdy, and G. J. Fryer, Structure of young oceanic crust at the East Pacific Rise near 9°30'N, *Geophys. Res. Lett., 19*, 1045-1048, 1992.

Creager, K. C., and L. M. Dorman, Location of instruments on the seafloor by joint adjustment of instrument and ship positions, *J. Geophys. Res.*, *87*, 8379-8388, 1982.

Detrick, R. S., P. Buhl, E. Vera, J. Mutter, J. Orcutt, J. Madsen, and T. Brocher, Multi-channel seismic imaging of a crustal magma chamber along the East Pacific Rise, *Nature*, *326*, 35-42, 1987.

Detrick, R. S., A. J. Harding, G. M. Kent, J. A. Orcutt, J. C. Mutter, and P. Buhl, Seismic structure of the southern East Pacific Rise, *Science*, *259*, 499-503, 1993.

Dijkstra, E. W., A note on two problems in connection with graphs, *Numer. Math.*, *1*, 269-271, 1959.

Fornari, D. J., M. R. Perfit, R. Batiza, and M. H. Edwards, Submersible transects across the East Pacific Rise crest and upper-flanks at 9°31'-32'N, 1, Observations of seafloor morphology and evidence for young volcanism off-axis (abstract), *Eos Trans. AGU*, *73* (43) Fall Meeting suppl., 525, 1992.

Goldstein, S. J., M. R. Perfit, R. Batiza, D. J. Fornari, and M. T. Murrell, Off-axis volcanism at the East Pacific Rise based on uranium-series dating of basalts, *Nature*, *367*, 157-159, 1994.

Harding, A. J., J. A. Orcutt, M. E. Kappus, E. E. Vera, J. C. Mutter, P. Buhl, R. S. Detrick, and T. M. Brocher, Structure of young oceanic crust at 13°N on the East Pacific Rise from expanding spread profiles, *J. Geophys. Res.*, *94*, 12,163-12,196, 1989.

Harding, A. J., G. M. Kent, and J. A. Orcutt, A multichannel seismic investigation of upper crustal structure at 9°N on the East Pacific Rise: Implications for crustal accretion, *J. Geophys. Res.*, *98*, 13,925-13,944, 1993.

Haymon, R. M., D. J. Fornari, M. H. Edwards, S. Carbotte, D. Wright, and K. C. Macdonald, Hydrothermal vent distribution along the East Pacific Rise crest (9°09-54'N) and its relationship to magmatic and tectonic processes on fast-spreading mid-ocean ridges, *Earth Planet. Sci. Lett.*, *104*, 513-534, 1991.

Hole, J. A., Nonlinear high-resolution three-dimensional seismic travel time tomography, *J. Geophys. Res.*, *97*, 6553-6562, 1992.

Humphreys, E. D., and R. W. Clayton, Tomographic image of the southern California mantle, *J. Geophys. Res.*, *95*, 19,725-19,746, 1990.

Jackson, D. D., The use of a priori data to resolve non-uniqueness in linear inversion, *Geophys. J. R. Aston. Soc.*, *57*, 137-157, 1979.

Kent, G. M., A. J. Harding, and J. A. Orcutt, Evidence for a smaller magma chamber beneath the East Pacific Rise at 9°30'N, *Nature*, *344*, 650-653, 1990.

Kent, G. M., A. J. Harding, and J. A. Orcutt, Distribution of magma beneath the East Pacific Rise between the Clipperton transform and the 9°17'N deval from forward modeling of common depth point data, *J. Geophys. Res.*, *98*, 13,945-13,969, 1993.

Kent, G. M., A. J. Harding, J. A. Orcutt, R. S. Detrick, J. C. Mutter, and P. Buhl, Uniform accretion of oceanic crust south of the Garrett transform at 14°15'S on the East Pacific Rise, *J. Geophys. Res.*, *99*, 9097-9116, 1994.

Koelsch, D. E., and G. M. Purdy, An ocean bottom hydrophone instrument for seismic refraction experiments in the deep ocean, *Mar. Geophys. Res.*, *4*, 115-125, 1979.

Koelsch, D. E., K. R. Peal, and G. M. Purdy, The Woods Hole Oceanographic Institution digital ocean bottom hydrophone instrument, *WHOI Tech. Rep.*, *82-30*, 15 pp., Woods Hole Oceanogr. Inst., Woods Hole, Mass., 1982.

Langmuir, C. H., J. F. Bender and R. Batiza, Petrological and tectonic segmentation of the East Pacific Rise, 5°30'-14°30'N, *Nature*, *322*, 422-429, 1986.

Lees, J. M., and R. S. Crosson, Tomographic inversion for three-dimensional velocity structure at Mount St. Helens using earthquake data, *J. Geophys. Res.*, *94*, 5716-5728, 1989.

Lowell, R. P., Modeling continental and submarine hydrothermal systems, *Rev. Geophys.*, *29*, 457-476, 1991.

Macdonald, K. C., P. J. Fox, L. J. Perram, M. F. Eisen, R. M. Haymon, S. P. Miller, S. M. Carbotte, M.-H. Cormier, and A. N. Shor, A new view of the mid-ocean ridge from the behaviour of ridge-axis discontinuities, *Nature*, *335*, 217-225, 1988.

Mattaboni, P. J., and S. C. Solomon, MITOBS: A seismometer system for ocean bottom earthquake studies, *Mar. Geophys. Res.*, *3*, 87-102, 1977.

McClain, J. S., J. A. Orcutt, and M. Burnett, The East Pacific Rise in cross section: A seismic model, *J. Geophys. Res.*, *90*, 8627-8639, 1985.

Menke, W., *Geophysical Data Analysis: Discrete Inverse Theory*, 260 pp., Academic, San Diego, Calif., 1984.

Moser, T. J., Shortest path calculation of seismic rays, *Geophysics*, *56*, 59-67, 1991.

Mutter, J. C., G. A. Barth, P. Buhl, R. S. Detrick, J. Orcutt, and A. Harding, Magma distribution across ridge-axis discontinuities on the East Pacific Rise from multichannel seismic images, *Nature*, *336*, 156-158, 1988.

Paige, C. C., and M. A. Saunders, LSQR: An algorithm for sparse linear equations and sparse least squares, *ACM Trans. Math. Software*, *8*, 43-71, 1982.

Perfit, M. R., M. C. Smith, D. J. Fornari, R. Batiza, and M. H. Edwards, Submersible transects across the East Pacific Rise crest and upper-flanks at 9°31'-32' N, 2, Small-scale spatial variations in lava geochemistry and implications for temporal variability (abstract), *Eos Trans. AGU*, *73* (43), Fall Meeting, suppl., 525, 1992.

Perfit, M. R., D. J. Fornari, M. C. Smith, J. F. Bender, C. H. Langmuir, and R. M. Haymon, Small-scale spatial and temporal variations in mid-ocean ridge crest magmatic processes, *Geology*, *22*, 375-379, 1994.

Shaw, P. R., and J. A. Orcutt, Waveform inversion of seismic refraction data and application to young Pacific crust, *Geophys. J. R. Astron. Soc.*, *82*, 375-414, 1985.

Sinton, J. M., and R. S. Detrick, Mid-ocean ridge magma chambers, *J. Geophys. Res.*, *97*, 197-216, 1992.

Solomon, S. C., and D. R. Toomey, The structure of mid-ocean ridges, *Annu. Rev. Earth Planet. Sci.*, *20*, 329-364, 1992.

Takanami, T., and G. Kitagawa, A new efficient procedure for the estimation of onset times of seismic waves, *J. Phys. Earth*, *36*, 267-290, 1988.

Tarantola, A., and B. Valette, Inverse problems = quest for information, *J. Geophys.*, *50*, 159-170, 1982.

Thurber, C. H., Earthquake locations and three-dimensional crustal structure in the Coyote Lake area, central California, *J. Geophys. Res.*, *88*, 8226-8236, 1983.

Tikhonov, A. N., and V. Y. Arsenin, *Solutions of Ill-posed Problems*, 258 pp., John Wiley, New York, 1977.

Toomey, D. R., and G. R. Foulger, Application of tomographic inversion to local earthquake data from the Hengill-Grensdalur central volcano complex, Iceland, *J. Geophys. Res.*, *94*, 17,497-17,510, 1989.

Toomey, D. R., G. M. Purdy, S. C. Solomon, and W. S. D. Wilcock, The three-dimensional seismic velocity structure of the East Pacific Rise near latitude 9°30'N, *Nature*, *347*, 639-645, 1990.

Um, J., and C. H. Thurber, A fast algorithm for two-point seismic ray tracing, *Bull. Seismol. Soc. Am.*, *77*, 972-986, 1987.

van der Sluis, A., and H. A. van der Vorst, Numerical solution of large, sparse linear algebraic systems arising from tomographic problems, in *Seismic Tomography*, edited by G. Nolet, pp. 49-83, D. Reidel, Boston, Mass., 1987.

Vera, E. E., and J. B. Diebold, Seismic imaging of oceanic layer 2A between 9°30'N and 10°N on the East Pacific Rise from two-ship wide-aperture profiles, *J. Geophys. Res.*, *99*, 3031-3041, 1994.

Vera, E. E., J. C. Mutter, P. Buhl, J. A. Orcutt, A. J. Harding, M. E. Kappus, R. S. Detrick, and T. M. Brocher, The structure of 0- to 0.2-m.y.-old oceanic crust at 9°N on the East Pacific Rise from expanded spread profiles, *J. Geophys. Res.*, *95*, 15,529-15,556, 1990.

Vidale, J. E., Finite-difference calculation of traveltimes in three dimensions, *Geophysics*, *55*, 521-526, 1990.

White, D. J., Two-dimensional seismic refraction tomography, *Geophys. J.*, *97*, 223-245, 1989.

Wiggins, R. A., The general linear inverse problem: Implication of surface waves and free oscillations for Earth structure, *Rev. Geophys.*, *10*, 251-285, 1972.

Wilcock, W. S. D., G. M. Purdy, S. C. Solomon, D. L. DuBois, and D. R. Toomey, Microearthquakes on and near the East Pacific Rise, 9°-10°N, *Geophys. Res. Lett.*, *19*, 2131-2134, 1992a.

Wilcock, W. S. D., S. C. Solomon, D. R. Toomey, and G. M. Purdy, The seismic attenuation structure of a fast-spreading mid-ocean ridge, *Science*, *258*, 1470-1473, 1992b.

Wilcock, W. S. D., D. R. Toomey, S. C. Solomon, and G. M. Purdy, The renavigation of Sea Beam bathymetric data between 9° and 10°N on the East Pacific Rise, *Mar. Geophys. Res.*, *15*, 1-12, 1993a.

Wilcock, W. S. D., M. E. Dougherty, S. C. Solomon, G. M. Purdy, and D. R. Toomey, Seismic propagation across the East Pacific Rise: Finite difference experiments and implications for seismic tomography, *J. Geophys. Res.*, *98*, 19,913-19,932, 1993b.

G. M. Purdy, Department of Geology and Geophysics, Woods Hole Oceanographic Institution, Woods Hole, MA 02543. (e-mail: mpurdy@cliff.whoi.edu).

S. C. Solomon, Department of Terrestrial Magnetism, Carnegie Institution of Washington, 5241 Broad Branch Rd. N. W., Washington, DC 20015. (e-mail: scs@clrs1.ciw.edu).

D. R. Toomey, 1272 Department of Geological Sciences, University of Oregon, Eugene, OR 97403-1272. (e-mail: drt@mazama.uoregon.edu).

(Received March 2, 1994; revised July 25, 1994; accepted July 27, 1994.)